FUNDAMENTAL UNDERSTANDING OF ELECTROOSMOTIC FLOW IN A HETEROGENEOUS CONVERGING-DIVERGING CIRCULAR MICROCHANNEL

By

Brandon Ewin Travis

Thesis

Submitted to the Faculty of the

Graduate School of Vanderbilt University in

partial fulfillment of the requirements

for the degree of

MASTER OF SCIENCE

in

Mechanical Engineering

December, 2008

Nashville, Tennessee

Approved:

Professor Haoxiang Luo

Professor D. Greg Walker

To the glory of God manifested in nature, upon which we are constantly looking. "The heavens declare the glory of God; And the firmament shows his handiwork." –Psalm 19:1

ACKNOWLEDGEMENTS

Several people have been instrumental in the production of this body of work and should be rightfully acknowledged here. First, to my wonderful parents Dennis and Kay Travis, unto whom I owe everything. Throughout my life they have raised me in a Christ-centered home and with wisdom, patience, and love have shaped me to be the person I am today. Always considering Proverbs 22:6, by example and principle they continually taught me to seek the will of God in all things and ardently follow the path He has set for my life. Mom and Dad, I love you and thank you.

Second, to my advisor Dr. Dongqing Li of whom I am greatly appreciative. Throughout his time as my advisor, Dr. Li has been especially supportive and gracious. He has always had an open door for me and been a prudent and wise advisor from which to draw counsel. I am quite thankful to him for bringing me to Vanderbilt University and was honored to work under his tutelage during his tenure here.

Third, to Dr. Haoxiang Luo for his guidance and above all else his friendly encouragement. Dr. Luo was extremely kind in taking me under his wing for several months and I am blessed to have been under his guidance.

Finally, many other people have been vast resources of knowledge, inspiration, support, and guidance; I am greatly esteemed to have been associated with these people: Barbaros Çetin, Ben Lewis, Dr. Chan Hee Chon, Dustin House, Hai Jiang, Nick Roberts, Dr. Nilanjan Sarkar, Suzanne Weiss, Xuan Weng, Xudong Wu, Yandong Gao, Yao Nan Wang, Dr. Yuejun Kang, and Dr. Zhemin Wu.

TABLE OF CONTENTS

Page

LIST OF FIGURES

Figure Page

Figure Page

Figure Page

LIST OF TABLES

Table Page

CHAPTER I

INTRODUCTION

In the last fifty years, many sections of the scientific and engineering communities have turned their attention to a newfound fascination: to that which is small. Beginning with Richard Feynman's landmark speech "There's Plenty of Room at the Bottom"[1], slowly at first and now with an ever-increasing pace scientific communities are looking at decreasing the length-scale and seeing what possibilities lie in the new frontier. It began first with electronics; the advent of the transistor gave rise to innumerable electronic possibilities, particularly microelectronic possibilities and the development of Moore's Law [2]. However, beginning en masse in the late 1980's and early 1990's, attention started shifting towards other possibilities on small scales. With the new micro-fabrication technologies made available because of microelectronics, the focus shifted to the world of fluid mechanics and a new area called "microfluidics". In 1989, Manz et al. [3] indicated that life sciences and chemistry would become the primary application fields of microfluidic technologies. Soon after, microfluidics found its use in a new area focusing on reducing laboratory sized processes on a small chip, thus the birth of lab-on-a-chip devices.

In use, LOC devices are designed to replicate the functions of their room-sized counterparts, consisting of a network of microchannels, electrodes, sensors, and other electronic devices on a small scale, as shown in Figure 1.1.

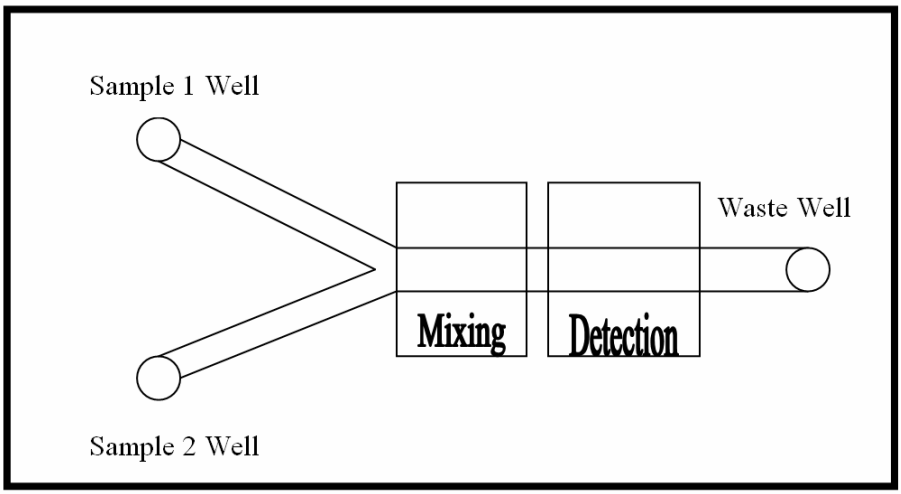

Figure 1.1. Basic lab-on-a-chip consisting of two samples being mixed and resultant sample being detected.

LOC devices have a wide range of functions and applications, be it micro-total analysis systems (μ-TAS) [4], PCR amplification [5], cell separation [6], electrochromatography [7], mixing [8], DNA analysis [9], cell manipulation [10], cell patterning [11], enzymatic reactions [12], immunoassay [13], molecular detection [14], heat exchangers [15], and pumps [16], amongst other uses.

Of chief concern in the field of microfluidics is how to operate these LOC devices, particularly what the driving mechanism in the microchannel will be to move the fluid along the length of the channel. Principally, there are two types of driving forces used in microchannels: pressure forces, and electrokinetic forces. Electrokinetic forces work simply by applying an electric field along the length of a microchannel, usually by placing electrodes of opposite charge in the wells of the microchannel. Electrokinetic phenomena can be broken down into four basic parts, as shown in Table 1.1.

Table 1.1. Classification of electrokinetic phenomena.

Name	Movement Description	Action
Electroosmosis	**Liquid moves relative to a stationary charged surface**	**Applied electric field used to induce movement**
Electrophoresis	Charged surface moves relative to a stationary liquid	Applied electric field used to induce movement
Streaming potential	Liquid moves relative to a stationary charged surface	Movement used to created an electric field
Sedimentation potential	Charged surface moves relative to a stationary liquid	Movement used to created an electric field

The idea of electroosmosis dates back to the research of F.F. Reuss who discovered the phenomena in 1809[17]. Initially, there was no fundamental understanding of how electroosmosis would be used in application, particularly because electroosmosis is quite impractical for macro-scale flow. However, with the reduction in the length scale electroosmosis proves to be quite useful in application.

Electroosmotic flow operates by moving liquid in a microchannel relative to a stationary charged surface. When a polar liquid, such as water, and a solid surface contact one another, an electric charge develops on the surface of the solid (for most microfluidic chips, this charge is negative). Ions of the opposite charge as the wall, called *counterions*, then migrate to the wall and form a layer several Angstroms thick called the *compact layer* (also referred to as the *Stern layer* in the literature). These counterions in the compact layer are stationary and do not move relative to the surface. However, just above the compact layer is another layer of ions, generally more counterions than *coions* (ions of the same charge as the wall) but a blend of the two, this layer being referred to as the diffuse layer (also called the *Gouy-Chapman* layer). The difference between the compact and diffuse layer is that the ions in the diffuse layer are moving, whereas those in the compact layer are not. The surface between the compact

layer and diffuse layer is called the *shear plane*, and the measure of electrical potential at the shear plane is called the *zeta potential*. The compact layer and the diffuse layer together are known as the electrical double layer (EDL) as shown in Figure 1.2.

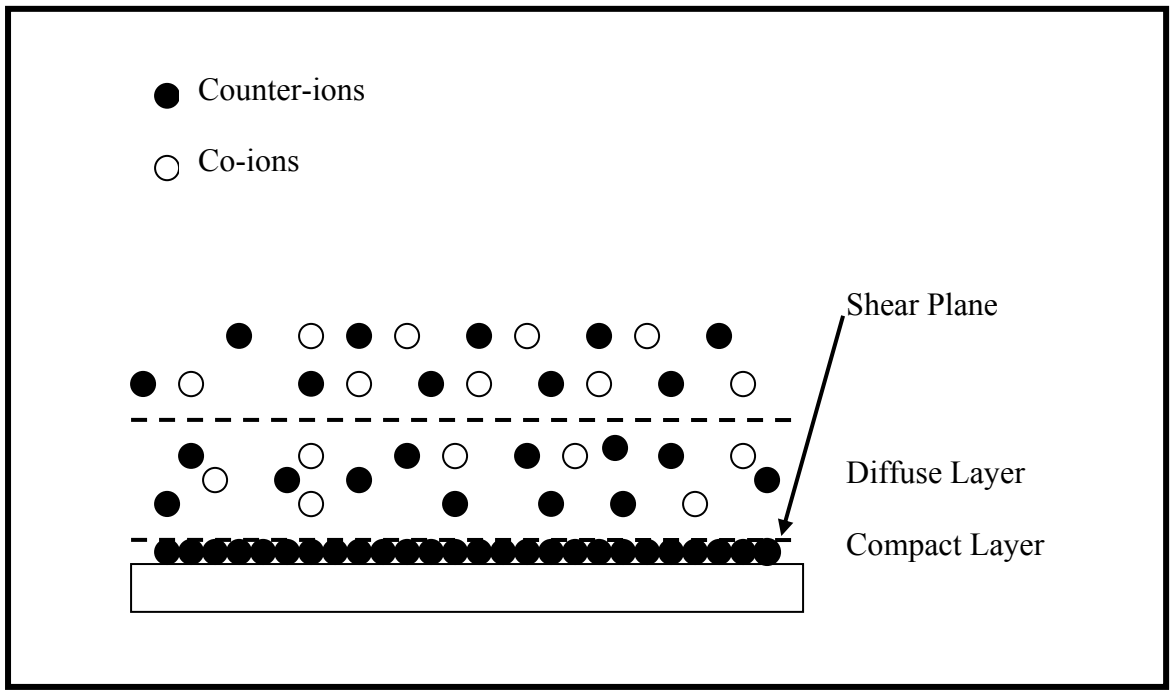

Figure 1.2. Electrical double layer inside a microchannel.

The EDL's thickness in a microchannel is independent of the solid surface material, but it is dependent on the properties of the fluid being used. Also, in general the thickness of the diffuse layer will be approximately 3 to 5 times that of the compact layer, and the overall thickness of the EDL decreases linearly as the bulk ionic concentration of the liquid increases. The zeta potential is an important parameter for electroosmotic flow because it has been shown that the velocity of the fluid in a microchannel is directly proportional to the zeta potential, an example of which is shown in Figure 1.3.

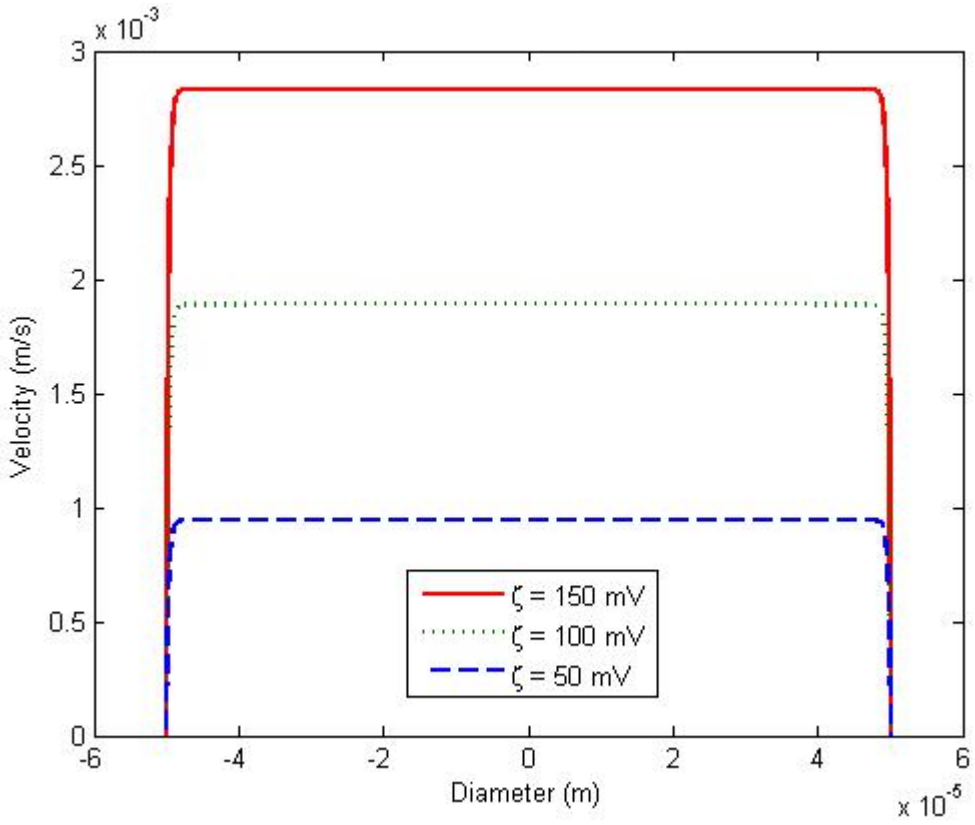

Figure 1.3. Velocity profile of electroosmotic flow in a sample circular capillary microchannel over a range of zeta potentials.

As can be seen, one of the unique properties of electroosmotic flow is the shape of velocity profile. Unlike pressure-driven flow with its parabolic shaped velocity profile, electroosmotic flow is considered "plug-like" flow with very little variation in the profile except near the EDL.

Electroosmotic flow in a converging-diverging heterogeneous microchannel was examined. Thus, the novelty of the research comes in the fact that we considered a unique geometry as well as considered a microchannel that has multiple zeta potentials, thus compounding the complexity of the work. Microchannel geometries vary greatly from device to device, depending on the function of the device. Electroosmotic flow has been modeled with many common shapes such as rectangular microchannels [18],

elliptical microchannels [19], T- and Y- shaped microchannels [20, 21, 22], as well converging-diverging microchannels [23]. Also, electroosmotic flow has been modeled in heterogeneous channels on several occasions before [24, 25, 26], the key reference to the topic coming from Herr et. al. [27]. Three different converging-diverging geometries were considered. The first geometry considered is shown in Figure 1.4.

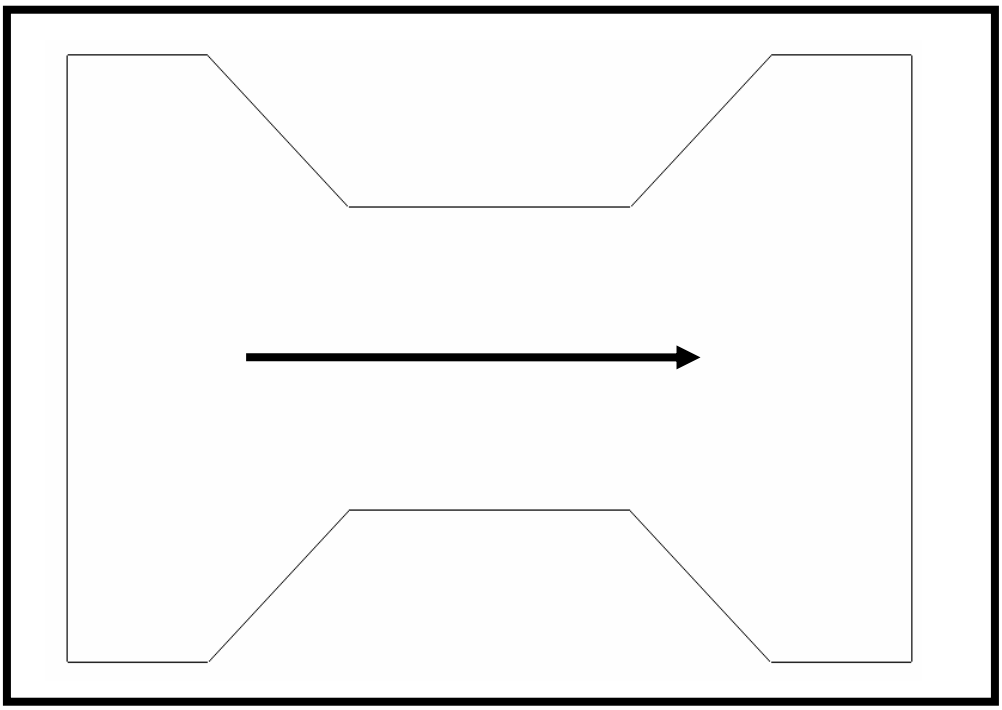

Figure 1.4. Geometry 1.

Geometry 1 was partitioned into three different sections: A, B, and C. Section A is the entrance and converging areas, section B is the constant cross-section area, and section C is the diverging and exit areas, as shown in Figure 1.5. The channel is dimensioned as shown in Figure 1.6.

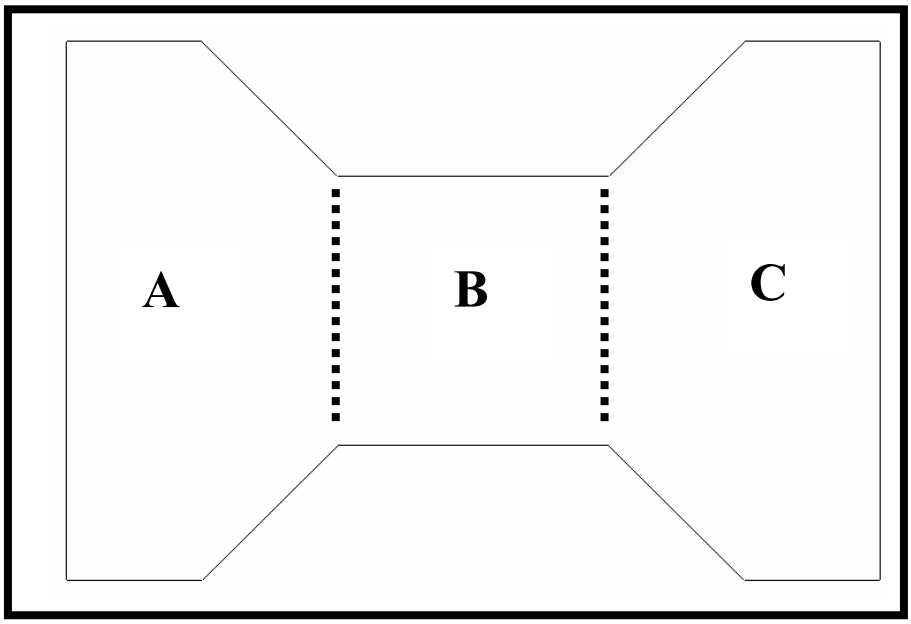

Figure 1.5. Geometry 1 with individual sections A, B, and C.

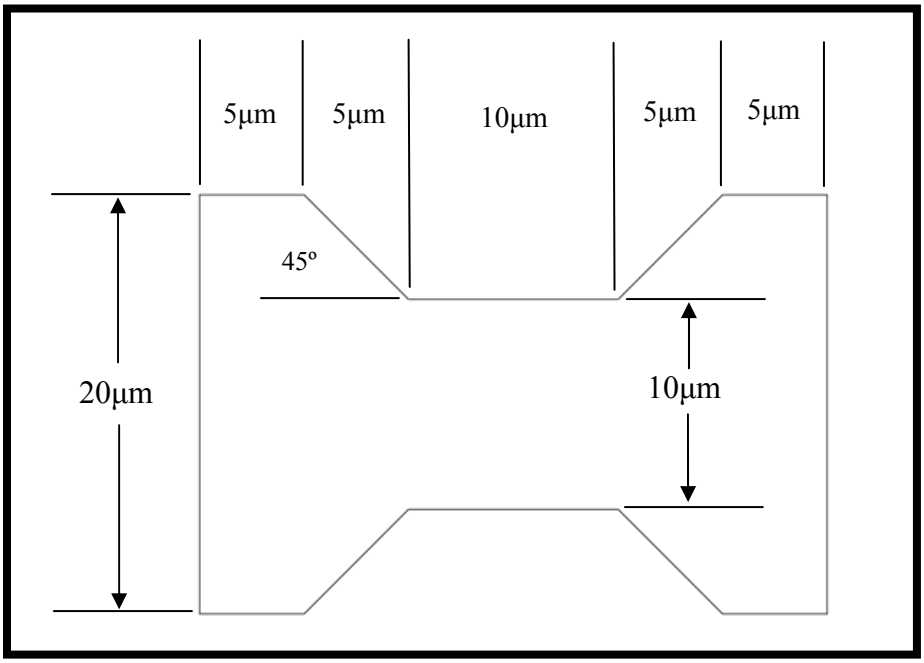

Figure 1.6. Dimensions of Geometry 1.

The second geometry considered is shown in Figure 1.7.

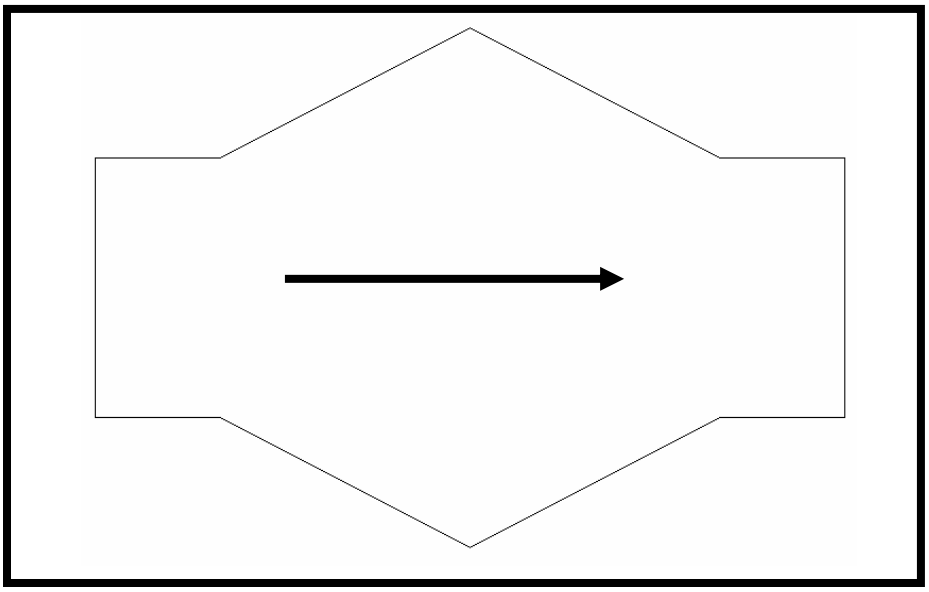

Figure 1.7. Geometry 2.

Geometry 2 was partitioned into two sections: A and B. Section A consisted of the entrance and diverging areas and section B consisted of the converging and exit areas, as shown in Figure 1.8; the microchannel was dimensioned as shown in Figure 1.9.

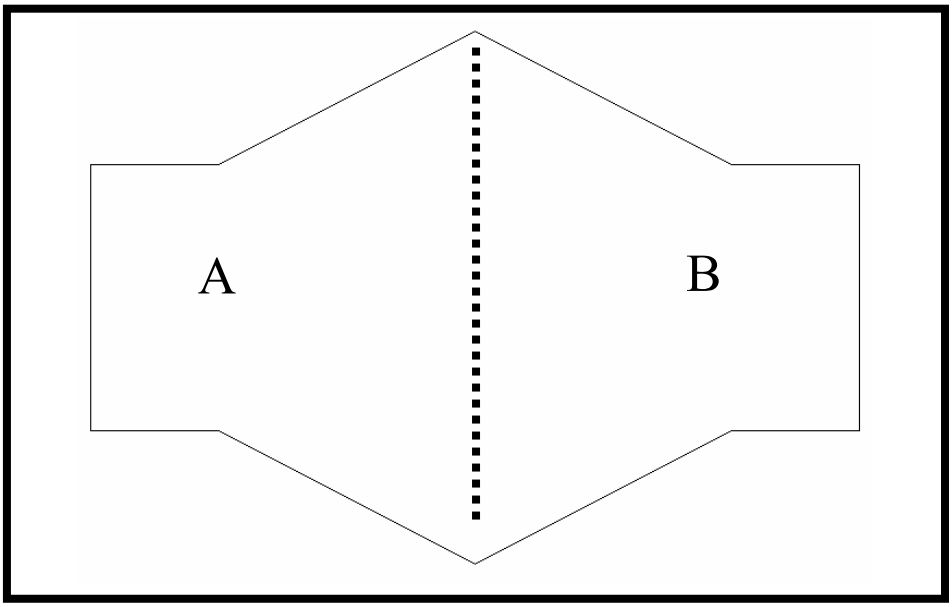

Figure 1.8. Geometry 2 with individual sections A and B.

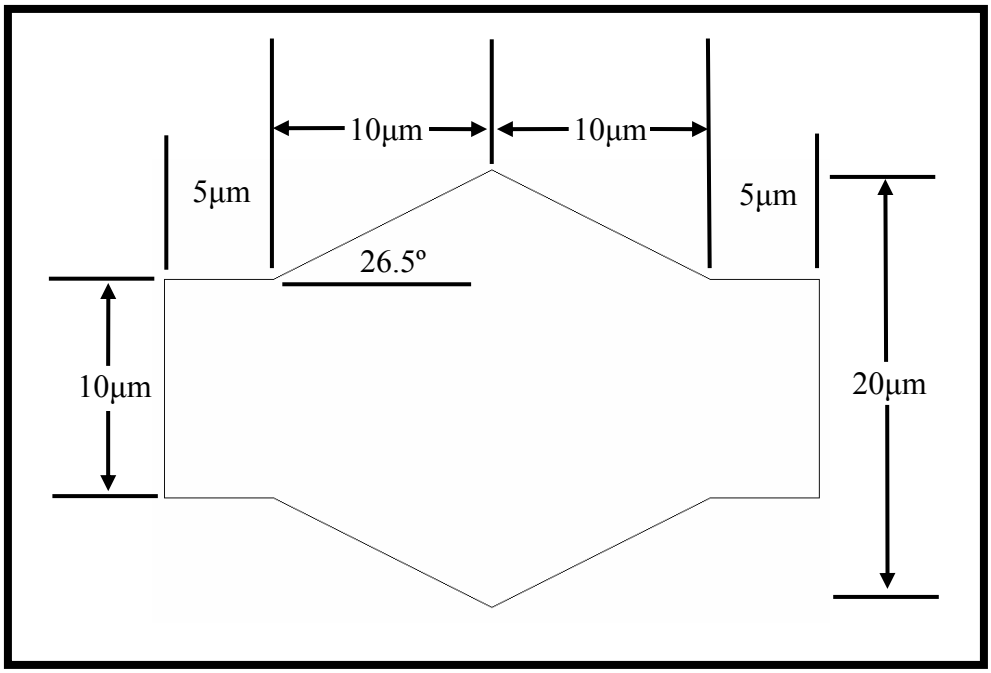

Figure 1.9. Dimensions of Geometry 2.

The third geometry considered is shown in Figure 1.10.

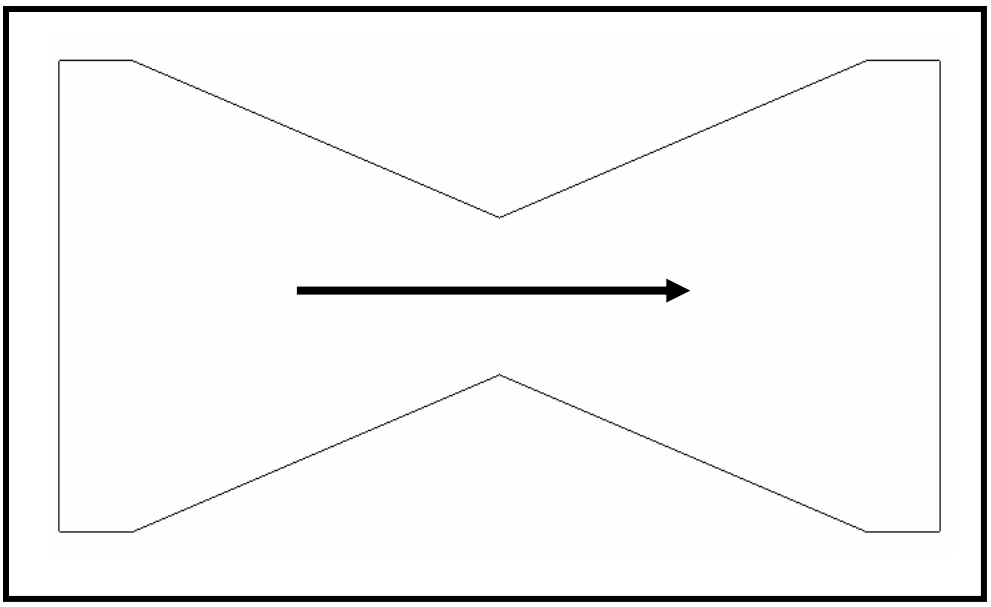

Figure 1.10. Geometry 3.

Geometry 3 was partitioned off into two sections: A and B. Section A consisted of the entrance and converging areas while section B consisted of the diverging and exit areas, as shown in Figure 1.11. Geometry 3 is dimensioned in Figure 1.12.

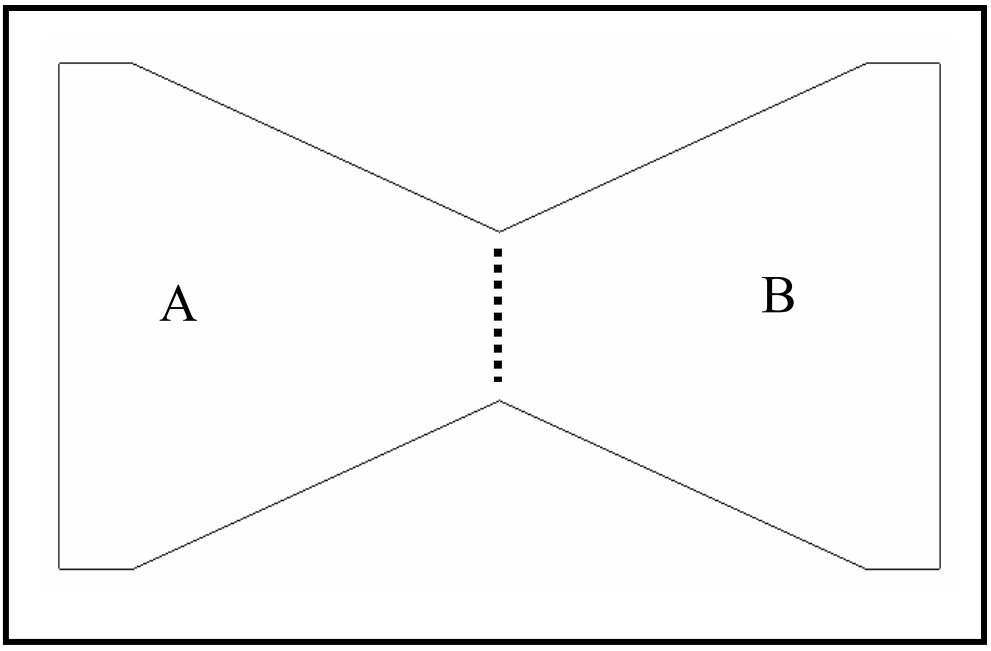

Figure 1.11. Geometry 3 with individual sections A and B.

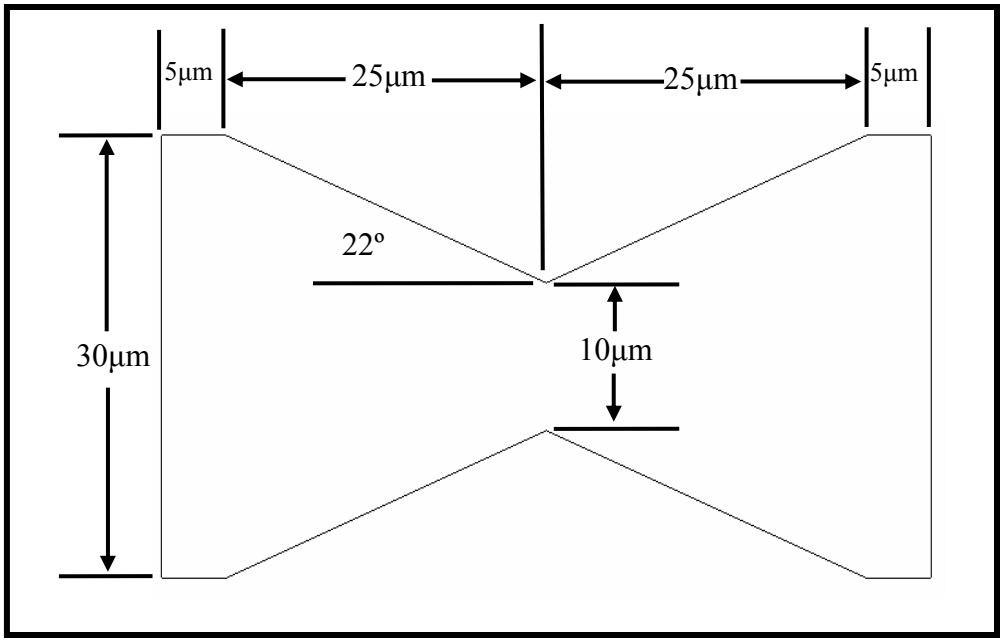

Figure 1.12. Dimensions of Geometry 3.

The effects of the applied electric field strength as well as the effects of several zeta potential conditions were examined for each geometry. First, the velocity profile in each section of each geometry was examined for three applied electric field strengths (10

V/cm, 50 V/cm, 100 V/cm). Second, the velocity profile in each section of each geometry was examined for several zeta potential conditions as follows:

Geometry 1: $\zeta_A = \zeta_B = \zeta_C$, $\zeta_A = -\zeta_B = \zeta_C$, $\zeta_{AC} / \zeta_B = 0.5$, $\zeta_B / \zeta_{AC} = 0.5$

Geometry 2 & 3: $\zeta_A = \zeta_B$, $\zeta_A = -\zeta_B$, $\zeta_A / \zeta_B = 0.5$, $\zeta_B / \zeta_A = 0.5$

Lastly, the streamlines for each geometry were examined for each zeta potential case listed above.

CHAPTER II

THEORY

Consider the flow of an incompressible Newtonian fluid in a cylindrical capillary as shown in Figure 2.1.

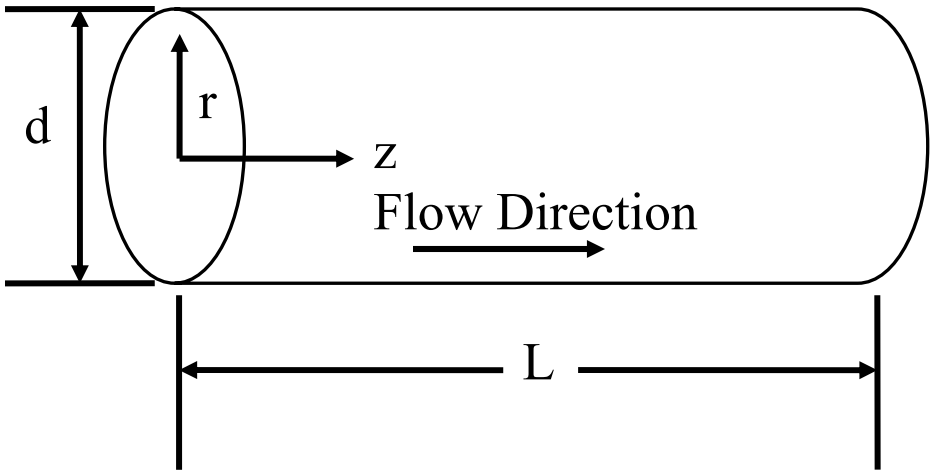

Figure 2.1. Cylindrical capillary with a radius r, diameter d, length L, and positive flow direction z.

In order to model this geometry, we first need to be able to model both the electrical double layer field in the channel as well as the electroosmotic flow field. We will establish the governing equations for each field, and then derive these equations using appropriate assumptions and defining applicable conditions that the model works for.

Electrical Double Layer

In adherence with the theory of electrostatics, the Poisson equation develops a relationship between the *electrostatic potential*, $\psi(r)$, and the *net charge density per unit volume*, ρ_e, at any point in the liquid, as shown in Equation 1,

$$\frac{1}{r}\frac{\partial}{\partial r}\left(r\frac{\partial \psi}{\partial r}\right) = -\frac{\rho_e}{\varepsilon\varepsilon_0} \tag{1}$$

where ε is the *dielectric constant* of the solution and ε_0 is the *permittivity of the vacuum*. With the application of the Boltzmann distribution, the ion number per unit volume in an electrolyte solution is shown in Equation 2,

$$n_i = n_{i\infty} \exp\left(-\frac{z_i e \psi}{k_b T}\right) \tag{2}$$

where $n_{i\infty}$ and z_i are the *bulk ionic concentration* and *valence of type i ion*, respectively, e is the charge of the proton, k_b is the *Boltzmann constant* and T is the *temperature*. The net volumetric charge density is given by Equation 3,

$$\rho_e(r) = \sum n_i z_i e = e\sum z_i n_{i\infty} \exp\left(-\frac{z_i e \psi}{k_b T}\right) \tag{3}$$

For a symmetric electrolyte solution the form becomes that of Equation 4,

$$\rho_e(r) = e\sum z_i n_{i\infty} \exp\left(-\frac{z_i e \psi}{k_b T}\right) = -2en_\infty \sinh\left(\frac{e\psi}{k_b T}\right) \tag{4}$$

Non-dimensional variables of use are Equations (5) and (6),

$$\psi^* = \frac{e\psi}{k_b T} \tag{5}$$

$$r^* = \frac{r}{d} \tag{6}$$

The non-dimensional variables can be used to rewrite the Poisson-Boltzmann equation as Equation (7),

$$\frac{1}{r^*}\frac{\partial}{\partial r^*}\left(r^*\frac{\partial \psi^*}{\partial r^*}\right) = \frac{2n_\infty e^2 d^2}{k_b T \varepsilon\varepsilon_0}\sinh\left(\psi^*\right) \tag{7}$$

Equation (7) is subjected to the boundary conditions of Equations (8) and (9),

$$r^* = 0 \qquad \frac{\partial \psi^*}{\partial r^*} = 0 \tag{8}$$

$$r^* = 0.5 \qquad \psi^* = \frac{e\zeta}{k_b T} \tag{9}$$

Electroosmotic Flow Field

The electroosmotic flow field can be fully described by the Navier-Stokes equations in cylindrical coordinates as shown in Equations 10, 11, and 12,

r-component

$$\rho\left(\frac{\partial v_r}{\partial t} + v_r\frac{\partial v_r}{\partial r} + \frac{v_\theta}{r}\frac{\partial v_r}{\partial \theta} - \frac{v_\theta^2}{r} + v_z\frac{\partial v_r}{\partial z}\right) = -\frac{\partial p}{\partial r} + \rho g_r + \mu\left[\frac{1}{r}\frac{\partial}{\partial r}\left(r\frac{\partial v_r}{\partial r}\right) - \frac{v_r}{r^2} + \frac{1}{r^2}\frac{\partial^2 v_r}{\partial \theta^2} - \frac{2}{r}\frac{\partial v_\theta}{\partial \theta} + \frac{\partial^2 v_r}{\partial z^2}\right] \tag{10}$$

θ-component

$$\rho\left(\frac{\partial v_\theta}{\partial t} + v_r\frac{\partial v_\theta}{\partial r} + \frac{v_\theta}{r}\frac{\partial v_\theta}{\partial \theta} - \frac{v_r v_\theta}{r} + v_z\frac{\partial v_\theta}{\partial z}\right) = -\frac{1}{r}\frac{\partial p}{\partial \theta} + \rho g_\theta + \mu\left[\frac{1}{r}\frac{\partial}{\partial r}\left(r\frac{\partial v_\theta}{\partial r}\right) - \frac{v_\theta}{r^2} + \frac{1}{r^2}\frac{\partial^2 v_\theta}{\partial \theta^2} - \frac{2}{r^2}\frac{\partial v_r}{\partial \theta} + \frac{\partial^2 v_\theta}{\partial z^2}\right] \tag{11}$$

z-component

$$\rho\left(\frac{\partial v_z}{\partial t} + v_r\frac{\partial v_z}{\partial r} + \frac{v_\theta}{r}\frac{\partial v_z}{\partial \theta} + v_z\frac{\partial v_z}{\partial z}\right) = -\frac{\partial p}{\partial z} + \rho g_z + \mu\left[\frac{1}{r}\frac{\partial}{\partial r}\left(r\frac{\partial v_z}{\partial r}\right) + \frac{1}{r^2}\frac{\partial^2 v_z}{\partial \theta^2} + \frac{\partial^2 v_z}{\partial z^2}\right] \tag{12}$$

From here, several assumptions can be made to simplify these equations. First, due to very low Reynolds numbers we can safely assume that no vorticity will take place, thus completely eliminating Equation 11 and all theta-dependent terms in Equations 10 and 12. Second, due to axial symmetry we know that the velocity will change only with respect to the z-direction (along the axis of the microchannel), thus leaving us only with

the z-component terms in conjunction with the continuity equation, as shown in Equation 13,

$$\mu \frac{1}{r} \frac{\partial}{\partial r} \left(r \frac{\partial v_z}{\partial r} \right) = \nabla P - E\rho_e \tag{13}$$

For homogeneous channels (constant zeta potential along the entire length of the channel) and channels without converging-diverging sections, we would normally be able to neglect the pressure gradient term in Equation 13. However, due to the geometry of our channel and particularly in heterogeneous cases, the pressure gradient term cannot be neglected. As was shown earlier, the zeta potential for a specific section directly influences the velocity in the section, and thus when a plurality of zeta potentials are introduced along the length of a channel, different sections will have different velocities. The differing velocities result in a pressure gradient occurring at the interface between the two sections, in some cases creating a suction of the flow and in other cases inhibiting the flow, depending on the conditions. For an incompressible liquid, continuity demands that the volumetric flow rates in all regions are equal; thus, the pressure gradients and their resultant effects must be accounted for.

Substituting Equation 4 for the net charge density into Equation 13 and introducing the non-dimensional variables shown in Equations 14 and 15,

$$u_z^* = \frac{u_z d}{D} \tag{14}$$

$$r^* = \frac{r}{d} \tag{15}$$

The full governing equation for the electroosmotic flow field in a channel is Equation 16,

$$\frac{1}{r^*} \frac{\partial}{\partial r^*} \left(r^* \frac{\partial u_z^*}{\partial r^*} \right) = \frac{2 n_\infty e d^3}{\mu D} E \sinh\left(\psi^*\right) + \frac{d^3}{\mu D} \frac{\partial p}{\partial z} \tag{16}$$

The microchannels used were assumed to be sufficiently long so that the flow at the inlet and outlet is fully developed and the flow pattern doesn't change along the channel at both the inlet and outlet. The electroosmotic flow field will be subjected to the inlet and outlet boundary conditions shown in Equation 17 and 18,

$$\frac{\partial u}{\partial z} = 0 \tag{17}$$

$$\frac{\partial p}{\partial z} = 0 \tag{18}$$

Also, because we will be modeling with low electric potential ($|\psi| \leq 25$ mV), the Debye-Huckel approximation shown in Equation 19 can be used,

$$\sinh \frac{ze\psi}{kT} \approx \frac{ze\psi}{kT} \tag{19}$$

Lastly, a note should made here concerning Joule heating. As we are dealing with electric fields, the potential of Joule heating effects (temperature increase in the channel due to a current passing through) are a real possibility. However, because our model uses low electric field strengths that induce a very low temperature increase (< 1ºC), it has been shown before by Çetin and Li [28] that Joule heating effects can be neglected.

CHAPTER III

MODEL

To solve the non-dimensional equation of motion for a converging-diverging microchannel (Equation 18), a solver software package called COMSOL Multiphysics was used. COMSOL's solver package allows us to analyze both the electric field and flow field simultaneously simply and easily. First, the shape for each geometry was modeled as a 2D axi-symmetric object, as shown in Figure 3.1.

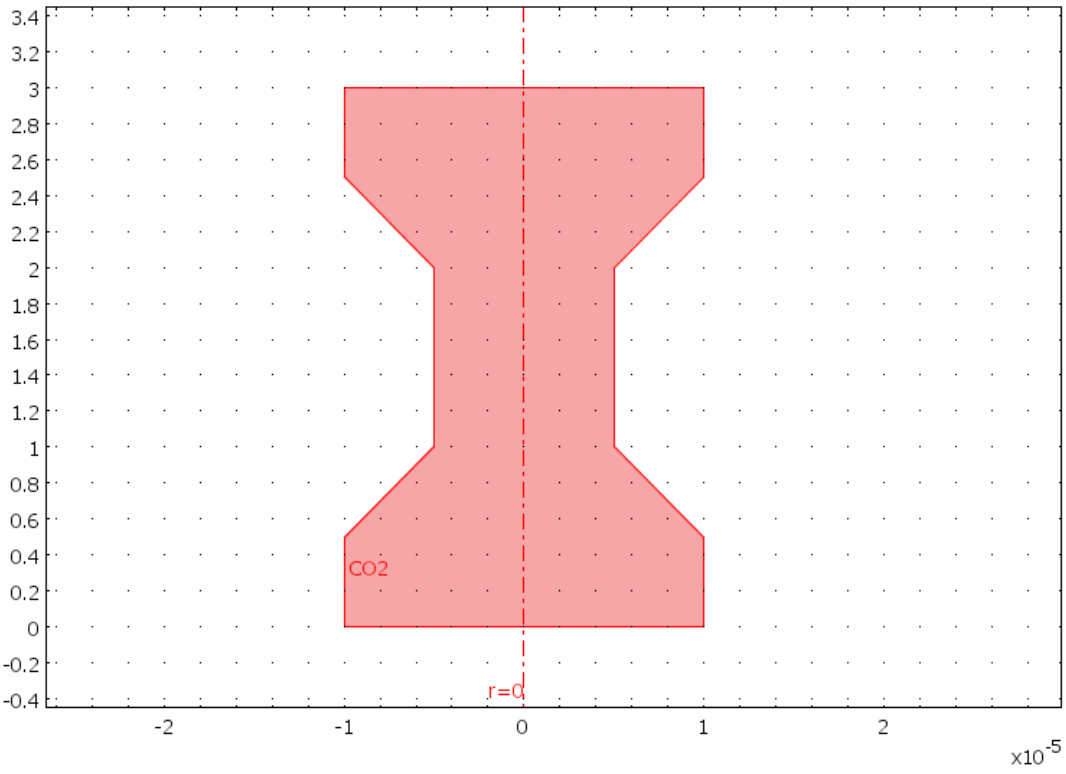

Figure 3.1. Completed Geometry 1 structure in COMSOL.

Next, the specific constants to be used for the calculations were established in COMSOL, as shown in Table 3.1.

Table 3.1. Simulation reference parameters.

Fixed Parameters	Symbol	Quantity	Unit
valence of ions	z	1	-
absolute temperature	T	298	kg/m s
dielectric constant	ε	78.5	C^2 / Nm^2
permittivity of free space	ε_0	8.85E-12	C^2 / Nm^2
elementary charge	e	1.60E-19	C
molarity of solution	M	1x10E-6	mol/L
Varied Parameters			
electric field strength	E	50, 100, 500	mV/m
zeta potential	ζ	10, -10, -20	mV
capillary diameter	d	10-20	μm

As can be seen from Table 3.1., the varied parameters were the electric field strength, zeta potential, and capillary diameter. In general, for a solid surface the zeta potential is dependent on the bulk ionic concentration, valence of the ions, and pH of the solution (pH has the ability to change the zeta potential from positive to negative). However, the zeta potential can also be altered by changing the microchannel surface material (e.g. from glass to PDMS) or by placing coatings on the microchannel wall.

After the key reference parameters were established, the boundary conditions for each case were established. For the electric field side, the walls of the microchannel were considered to be electric insulation and the outlet was considered to be grounded. The inlet to the microchannel was established as an electric potential, and the value that was set was dependent upon the desired electric field strength. All boundary settings are shown in Figure 3.2.

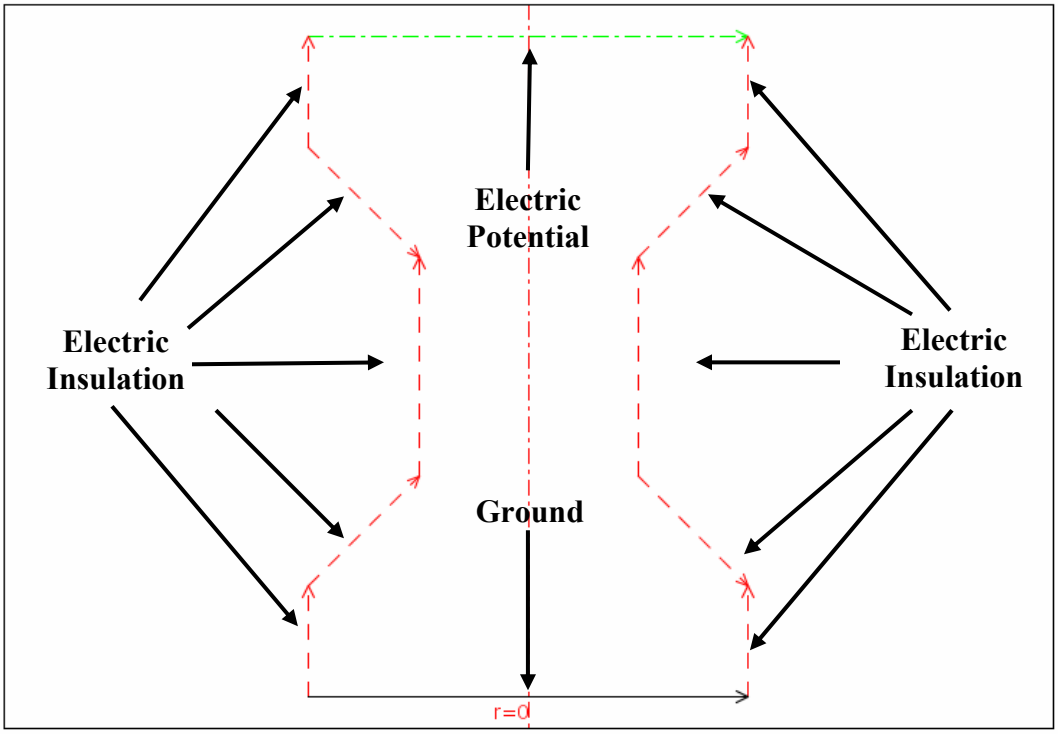

Figure 3.2. Boundary settings for the electrical field in the microchannel.

Next, the boundary conditions were established for the electroosmotic flow field. Typically, the boundary conditions for EOF would be set as no-slip due the velocity at the wall (compact layer) being zero with the velocity magnitude increasing sharply as it moves through the diffuse layer and then finally a flat profile across the channel (see Figure 1.3.). However, because the thickness of the EDL is much smaller than the diameter of the channel, it can be neglected.

If the EDL is thin relative to the channel dimensions, the *Helmholtz-Smoluchowski equation* can be used. The Helmholtz-Smoluchowski originates from the simplified version of the Poisson-Boltzmann equation, as shown in Equation 20,

$$\mu \nabla^2 u_{EOF} = \varepsilon E \frac{d^2 \phi^2}{dr^2} \tag{20}$$

where u_{EOF} is considered to be the component of the flow due to electroosmosis. If the flow is fully developed, the only gradients that will be present are those in the r direction, so the equation becomes Equation 21,

$$\mu \frac{d^2 u_{EOF}}{dr^2} = \varepsilon E \frac{d^2 \phi^2}{dr^2} \tag{21}$$

The differential equation can be solved by two integrations with respect to r and application of appropriate boundary conditions (at edge of EDL, fluid velocity and potential equal to zero, at the wall the potential is set equal to the zeta potential of the wall). Thus, the Helmholtz-Smoluchowski is shown in Equation 22,

$$u_{EOF} = \frac{\varepsilon E \zeta}{\mu} \tag{22}$$

The application of the Helmholtz-Smoluchowski is subject to the restriction that the EDL is thin relative to the channel dimension. Equation 22 was applied at the microchannel walls for each geometry.

The inlet and outlet of the microchannel were established with the boundary conditions established in Equations 17 and 18, with consideration that the microchannel is sufficiently long so that flow in the inlet and outlet is fully developed.

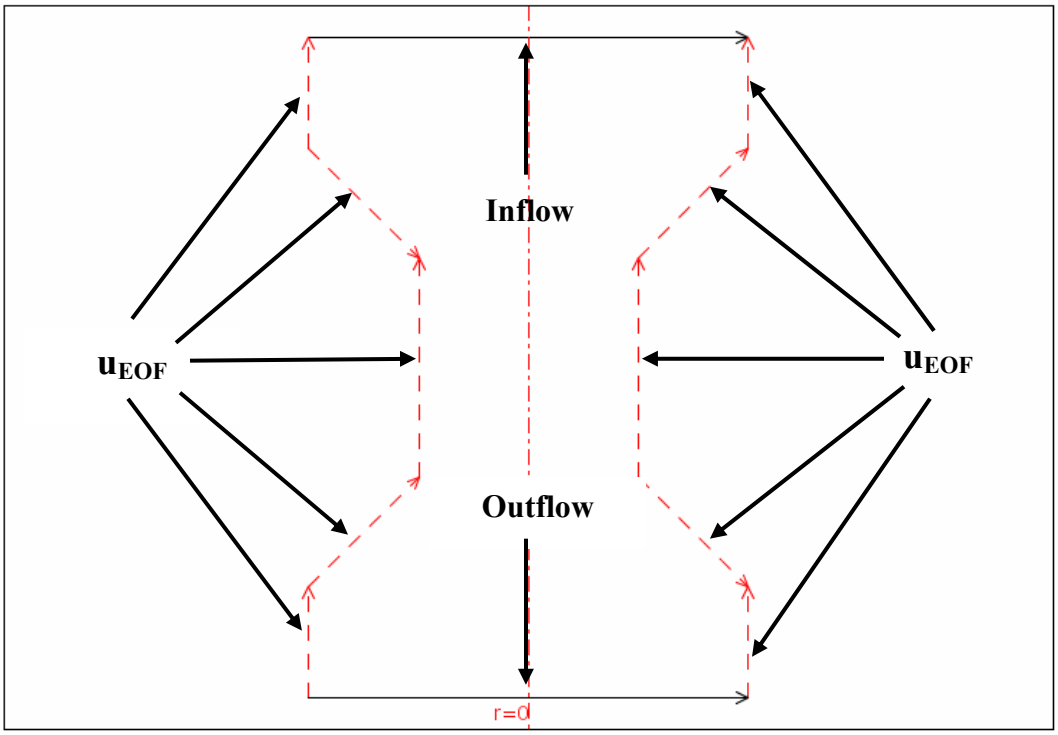

Figure 3.3. Electroosmotic flow field boundary settings.

After all boundary settings were selected, the geometry was meshed using a fine triangular mesh (usual minimum element qualities were between 0.6 and 0.8) as shown in Figure 3.4.

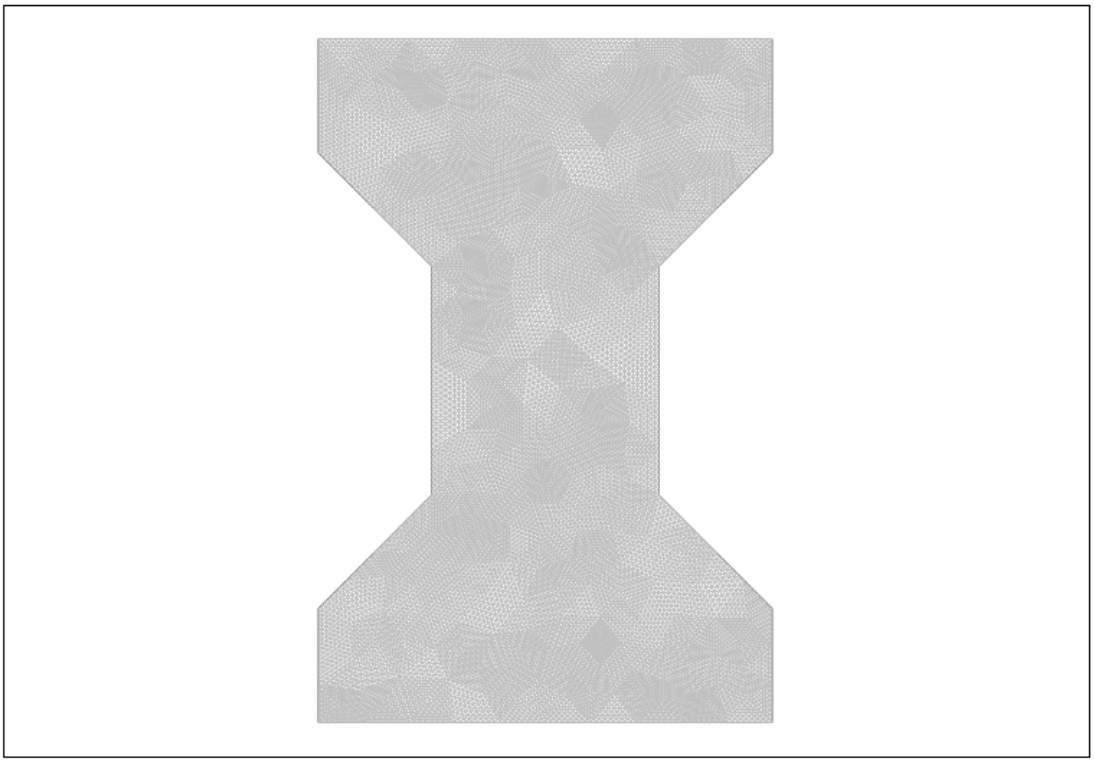

Figure 3.4. Geometry 1 mesh.

A grid check was then performed for each mesh to ensure grid independence of the results, with the results showing a nice conformance for the mesh used. Figures 3.5, 3.6, and 3.7 show the result of a sample grid check on Geometry 1 in section A. Grid checks in all other locations and geometries were comparable.

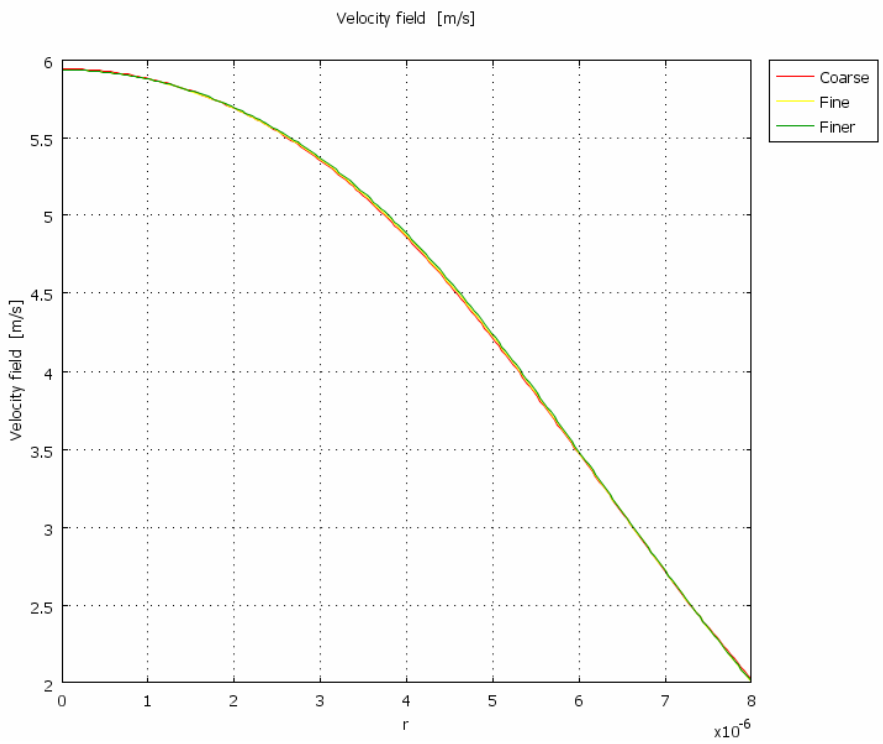

Figure 3.5. Grid check of Geometry 1 in section A.

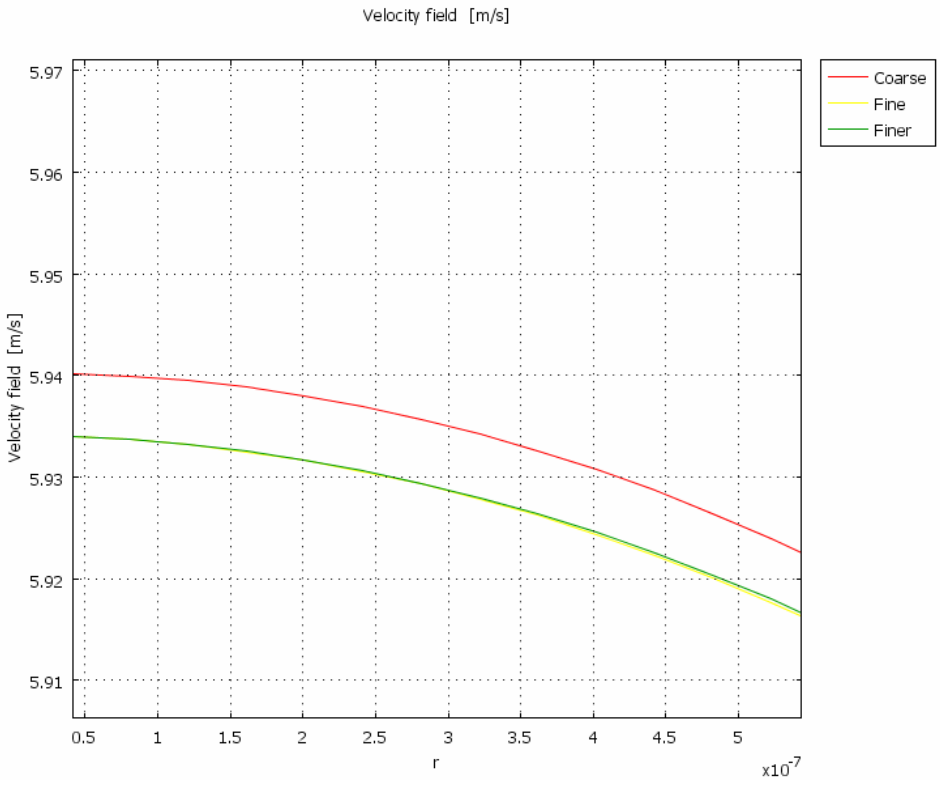

Figure 3.6. Zoom of velocity magnitude of Geometry 1 in section A.

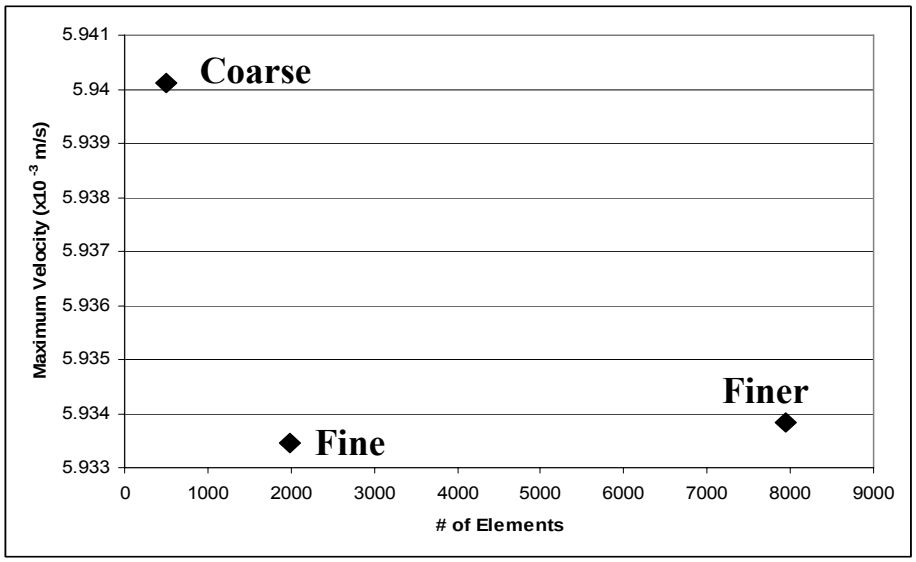

Figure 3.7. Comparison of maximum velocities for three mesh sizes.

After the grid check was performed, the model was then solved using COMSOL's stationary non-linear equation solver and results were acquired. The process was repeated for Geometries 2 and 3 with identical boundary settings on both the electrical field and electroosmotic flow field as those used for Geometry 1.

To verify the accuracy of the model, a cylindrical microchannel was constructed with the same boundary settings as described above but using the dimensions and parameters used by Li [29]. The results show good agreement with Li's results, as well as good agreement with the calculated velocity (using Equation 22) of 4.205×10^{-3} m/s.

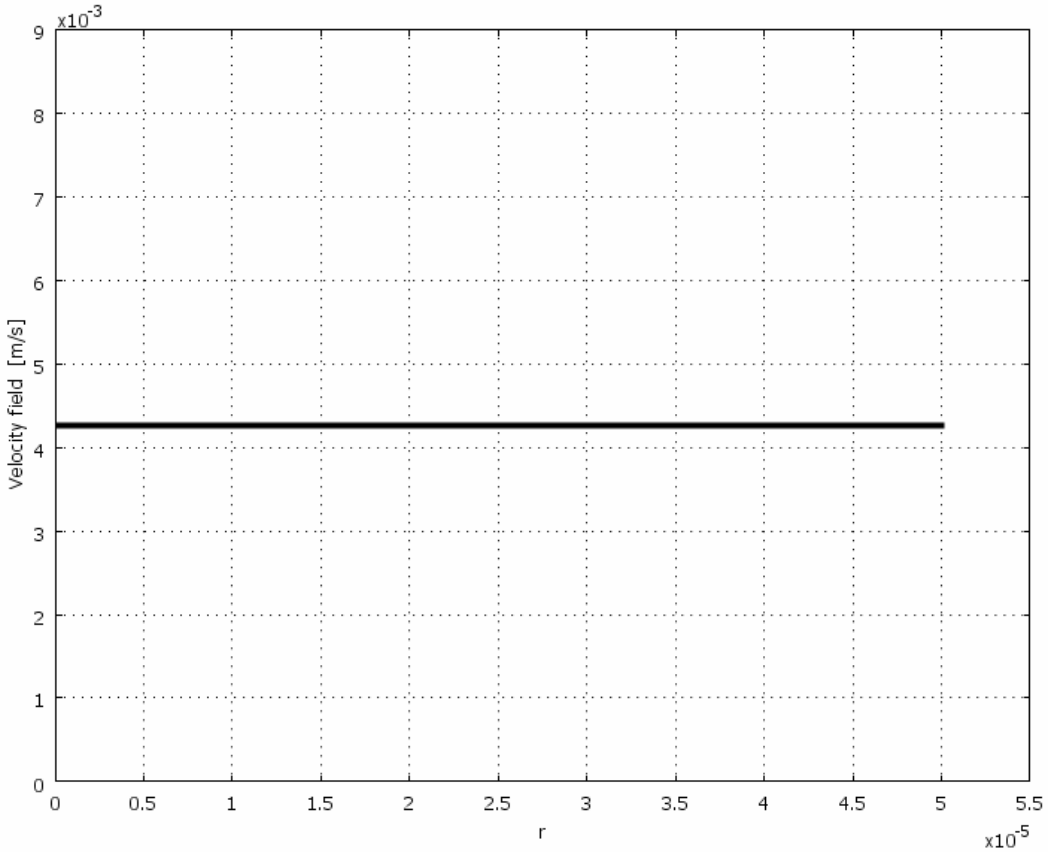

Figure 3.8. The electroosmotic flow velocity field of a symmetric electrolyte solution in a cross-section of a cylindrical microchannel of 100 μm in diameter with ζ = -200 mV. The applied field strength is 300 V/cm.

CHAPTER IV

RESULTS

Geometry 1

Geometry 1 consisted of a microchannel with a converging (nozzle) section at the entrance to the microchannel (section A), followed by a cylindrical section of constant area (section B), ending with a diverging (diffuser) section at the outlet (section C). The first simulation performed on the geometry was to consider the effects of electrical field strength on the velocity profile. Velocity profiles were generated at the midplane of sections A and B, as shown in Figures 4.1. and 4.2.

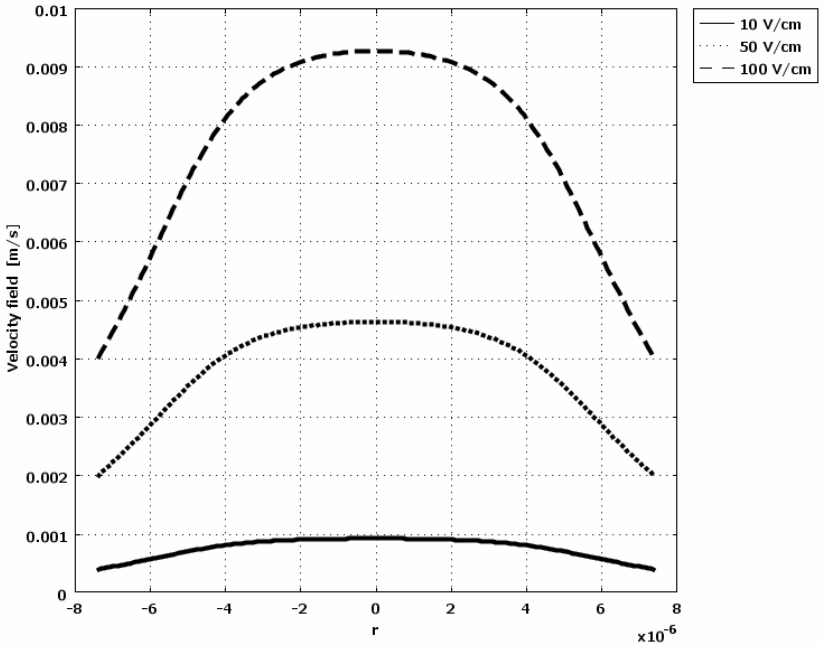

Figure 4.1. Velocity profile of Geometry 1 measured in section A for various electric field strengths with ζ = -100 mV.

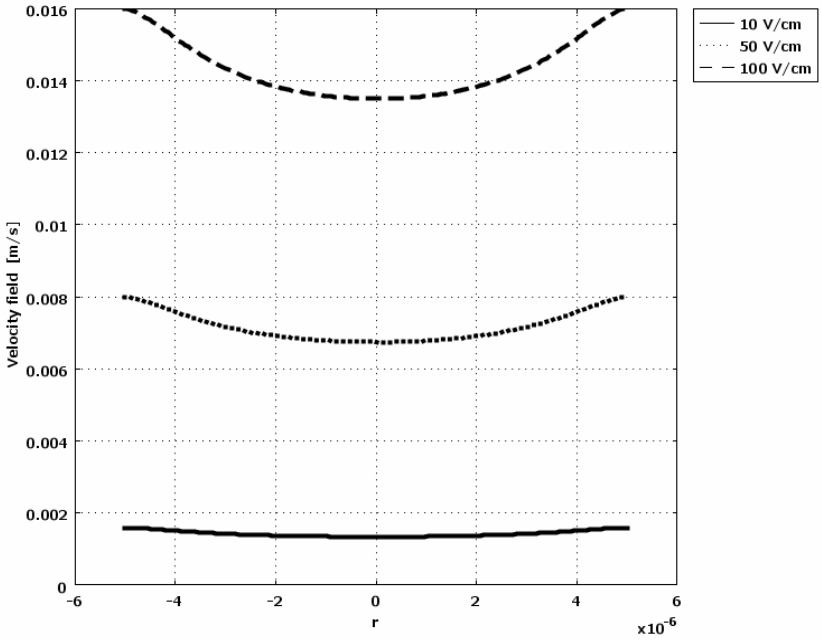

Figure 4.2. Velocity profile of Geometry 1 measured in section B for various electric field strengths with ζ = -100 mV.

As can be seen from both figures, a proportional increase occurs in the magnitude of the velocity in relation to the applied electric field. Thus, doubling the applied electric field strength doubles the magnitude of the velocity and vice-versa. However, it should be noted, particularly in Figure 4.2., how much the pressure gradient plays a key role in the shape of the profile. Due to decreased cross-sectional area in section B, the pressure has thus increased in the section and produces a pressure gradient along the length of the microchannel (thus electroosmotic flow coupled with pressure-driven flow). As has been shown earlier, pure EOF produces plug-shaped velocity profiles that are flat on the top. However, as can be clearly seen, Figure 4.2. resembles more of the parabolic shape of pressure-driven flow than that of EOF. Thus, it can be deduced that the pressure gradient (and thus the shape of the microchannel that produces the pressure gradient) plays a significant role on the velocity of the fluid in the microchannel.

Next, let's look at the velocity profiles for Geometry 1 for various applied zeta potentials, first for section A in Figure 4.3.

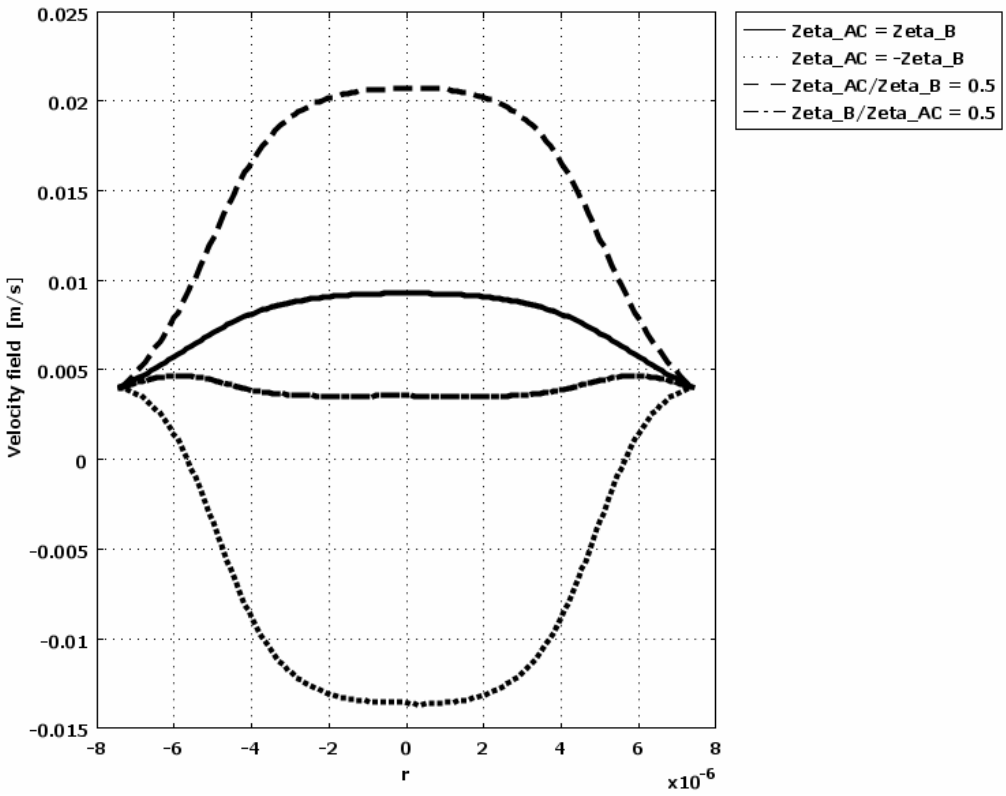

Figure 4.3. Velocity profile of Geometry 1 measured in section A for various zeta potentials, E = 100 V/cm.

The key to understanding the shapes produced for each section is to understand the balance between pressure-driven flow and EOF. First, when the channel is homogeneous (zeta potential constant) we see a similar profile as to what was shown in Figure 4.1. However, when the zeta potential is doubled in section A to that of section B, we see an increase in the magnitude of the velocity relative to the increase in zeta potential. Even more interesting though, when the zeta potential in section B is doubled to that of section A, the velocity magnitude is the highest of the group, yet the shape of the profile is a negative bell curve. This shows the influence of suction coming from section B due to both the pressure gradient in the section as well as the increasing zeta potential.

Likewise, when the zeta potential in each section is reversed, suction also occurs due to the zeta potential but the effect of the pressure gradient is much greater than that of zeta potential, and thus the velocity magnitude is lower than the rest of the group. Again, these plots show the effect that the pressure gradient has due to the channel being heterogeneous, and how this plays a bigger role than the EOF. Figure 4.4. shows the velocity profile in section B under the same conditions.

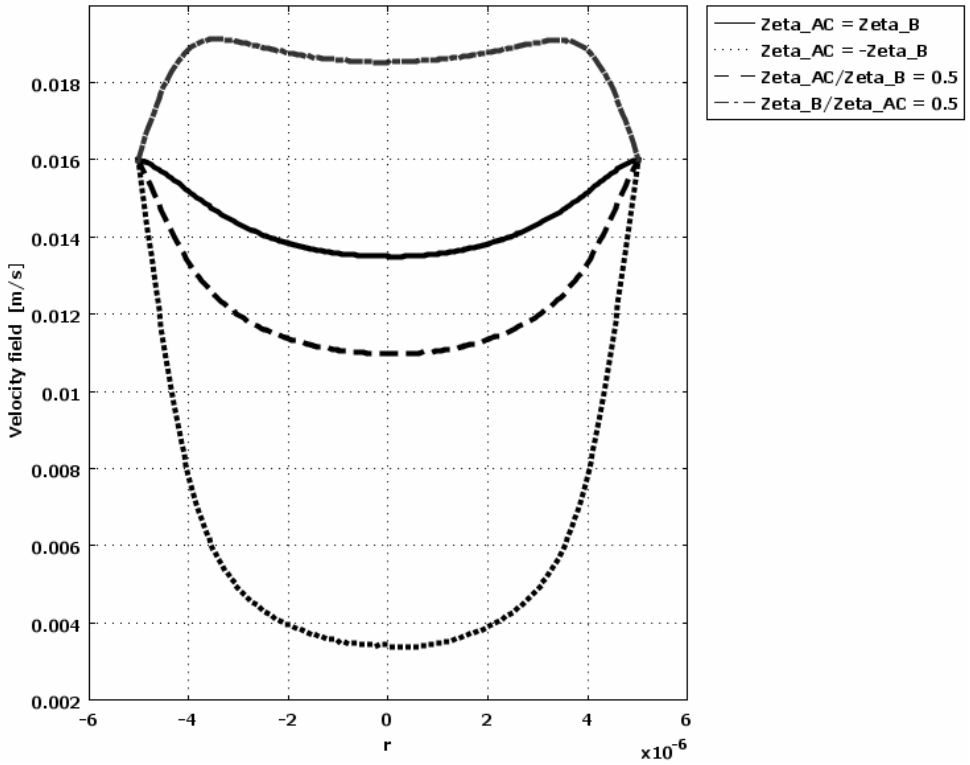

Figure 4.4. Velocity profile of Geometry 1 measured in section B for various zeta potentials, E = 100 V/cm.

From Figure 4.4., we see again that when the channel is homogeneous, the profile is bell-shaped in nature and under great influence of the increased pressure due to the microchannel dimensions. When these channel dimensions are coupled with an increase in zeta potential in section B (thus section B's zeta potential is double that of section A and C), the velocity magnitude is greatly increased. However, when zeta potential in

section B is lower than that of section A/C or opposite of that in A/C, a battle takes place between pressure gradients of opposing forces which in turn will cause eddy's to be generated in the channel (see Figure 4.8.). Again, the general theme is the importance of pressure gradients in the channel relative to the electrokinetic forces.

Next, let's look at the streamline and arrow plots of Geometry 1 under a variety of zeta potential cases, as shown in Figures 4.5-4.12.

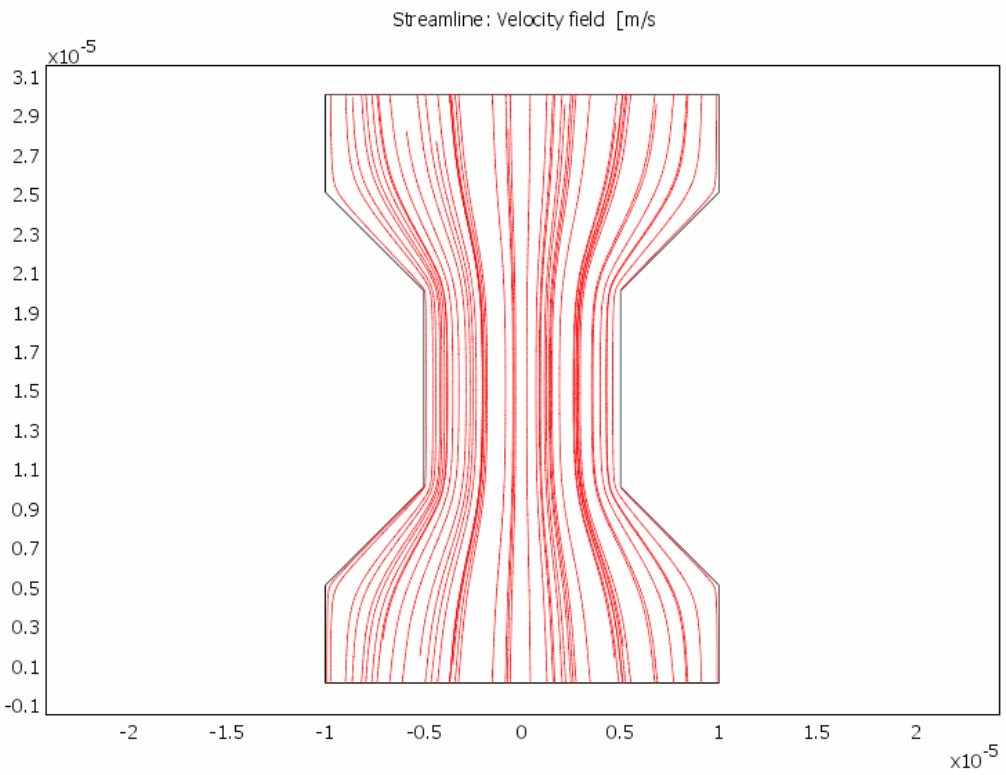

Figure 4.5. Streamlines of Geometry 1 in a homogeneous microchannel.

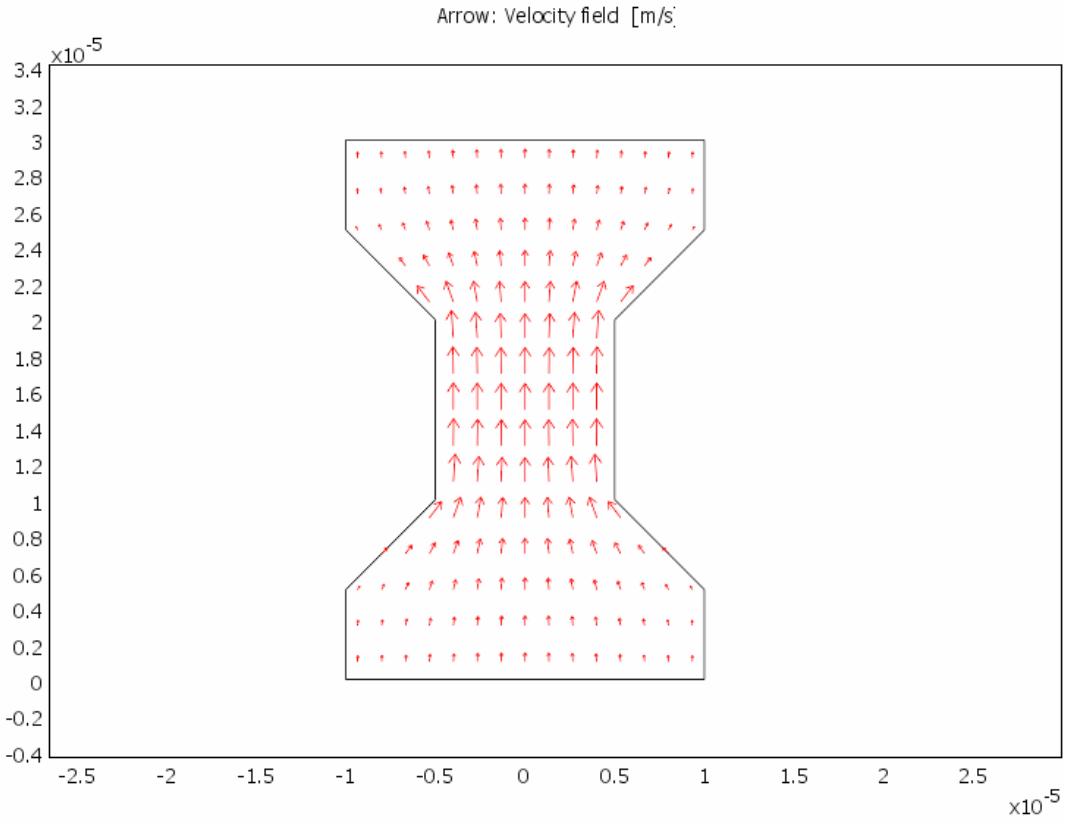

Figure 4.6. Arrow plot of Geometry 1 in a homogeneous microchannel.

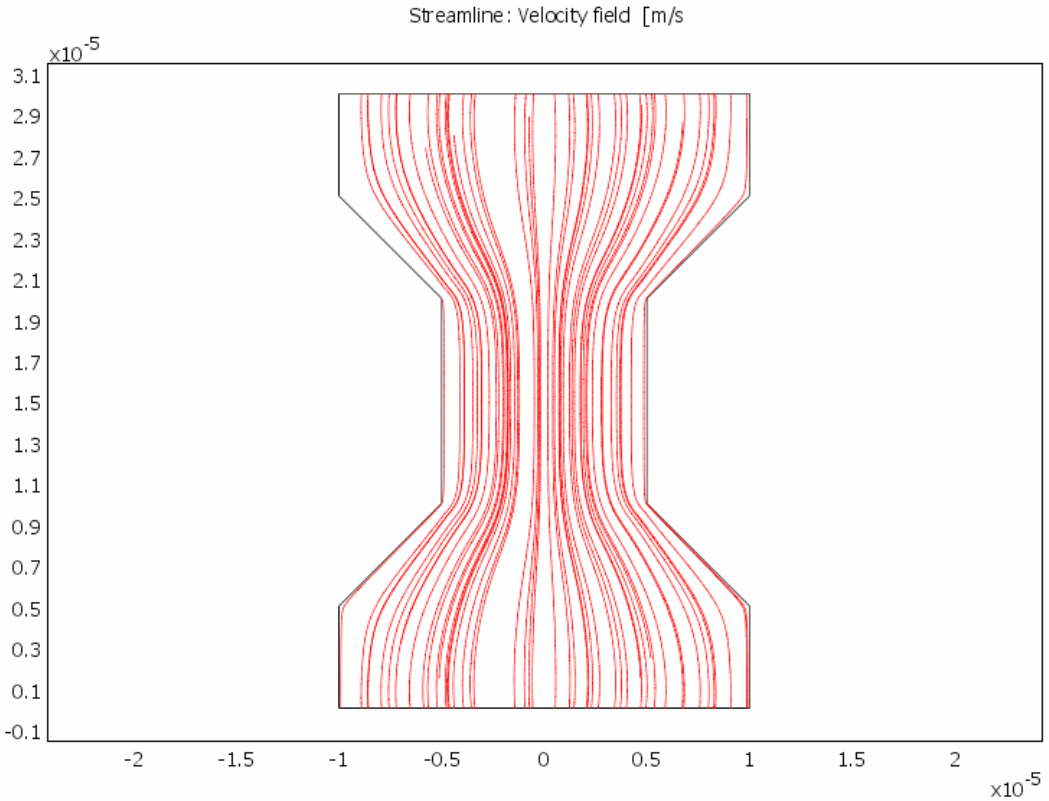

Figure 4.7. Streamlines of Geometry 1 with $\zeta_{AC}/\ \zeta_B = 2$.

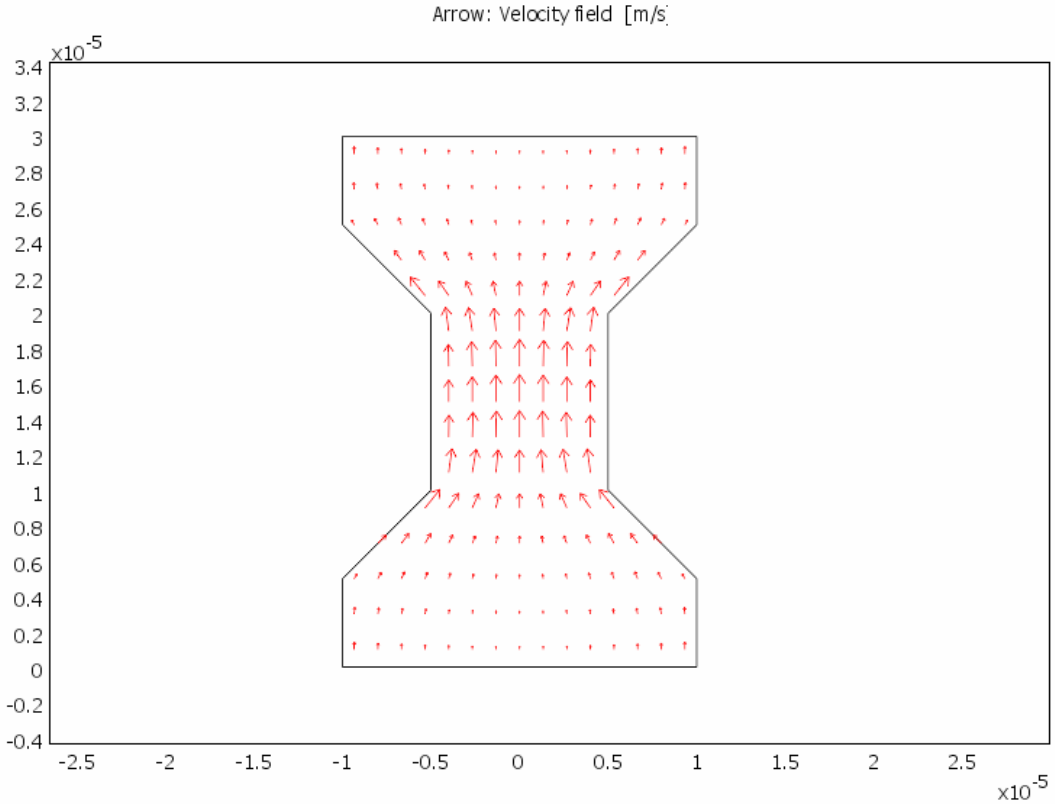

Figure 4.8. Arrow plot of Geometry 1 with $\zeta_{AC}/\ \zeta_B = 2$.

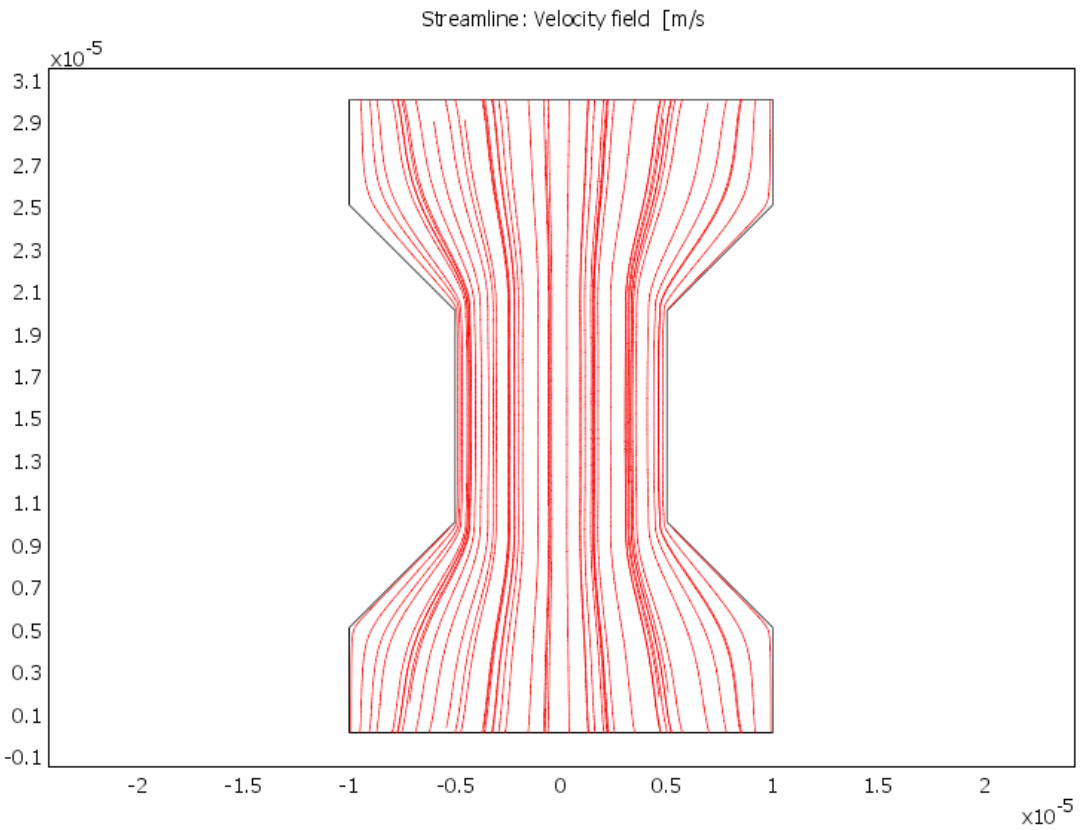

Figure 4.9. Streamlines of Geometry 1 with $\zeta_{AC}/\ \zeta_B = 0.5$.

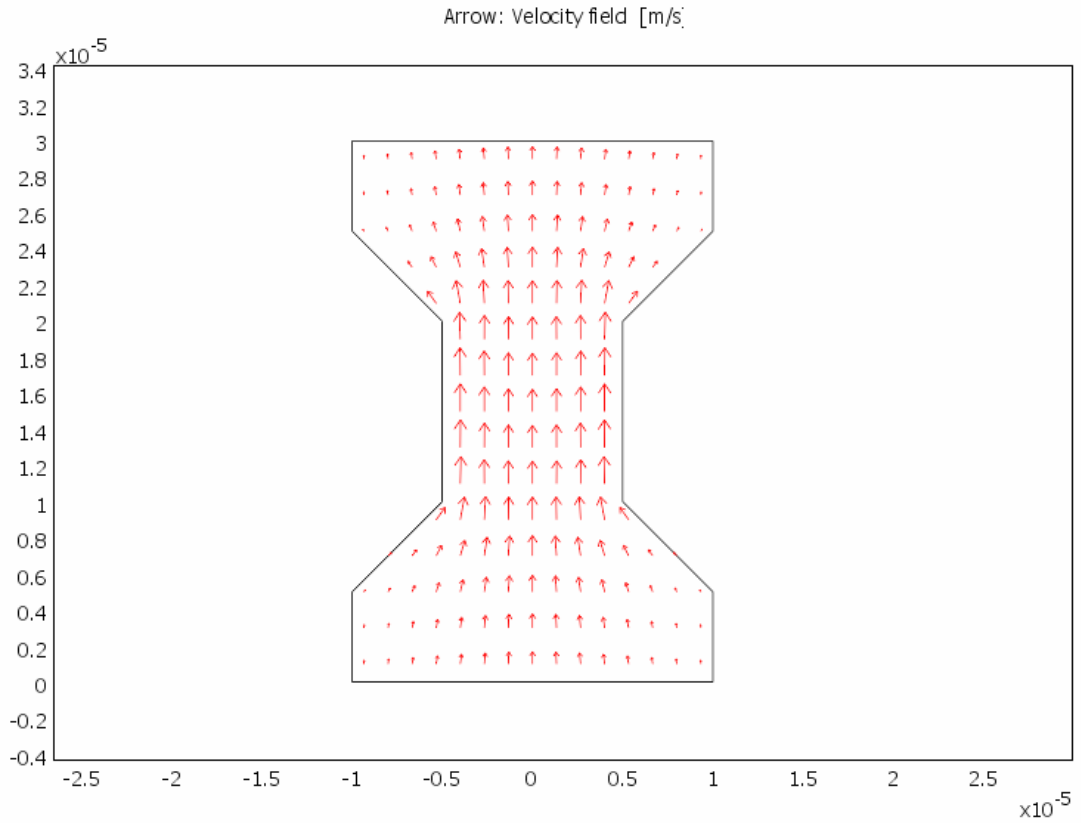

Figure 4.10. Arrow plot of Geometry 1 with $\zeta_{AC}/\ \zeta_B = 0.5$.

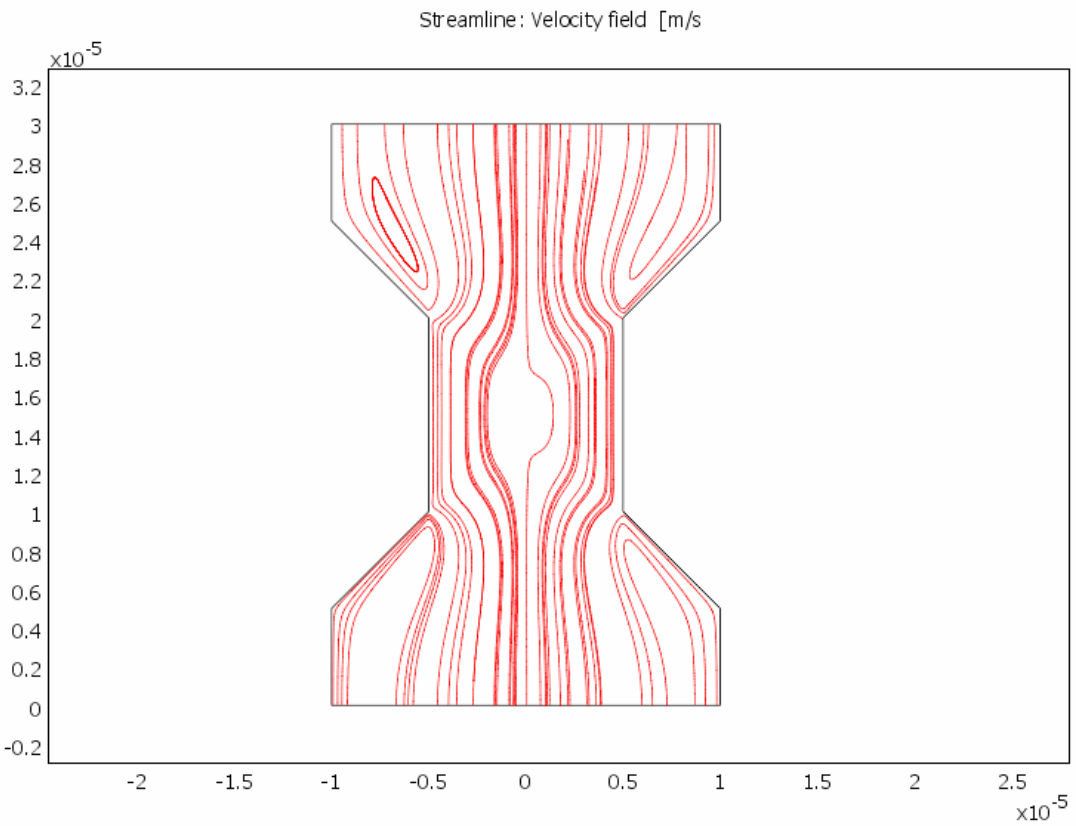

Figure 4.11. Streamlines of Geometry 1 with $\zeta_{AC} = -\zeta_B$.

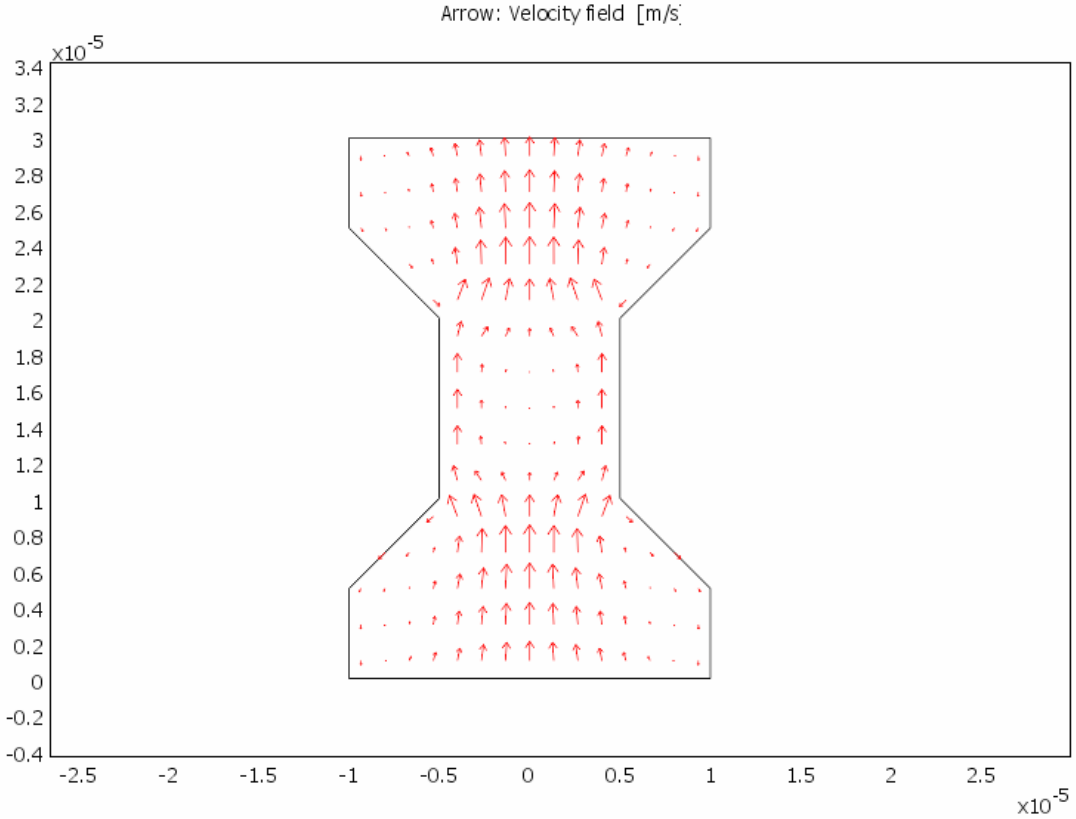

Figure 4.12. Arrow plot of Geometry 1 with $\zeta_{AC} = -\zeta_B$.

Figures 4.5, 4.7, and 4.9 show the same streamline plots, indicating that despite the different magnitudes of the zeta potential that the fluid follows along essentially the same path. However, when the zeta potential is reversed as shown in Figure 4.11, eddy's are produced in sections A and C that result in zero net flow in the corners of the channel. However, there is still positive net flow through the channel as the eddy's created due to zeta potential difference due not inhibit the flow completely. Flow rates for Geometry 1 under various applied electric field strengths are shown in Table 4.1., as well as reference flow rates (cylindrical microchannel with a constant diameter of 20 μm). Flow rates for Geometry 2 under the various zeta potential conditions are shown in Table 4.2.

Table 4.1. Flow rates for Geometry 1 under various applied electric field strengths with ζ = -100 mV, as well as reference geometry results.

E (V/cm)	G1 Q (mm^3/s)	Reference Q (mm^3/s)
10	1.414E-04	2.20E-04
50	5.655E-04	1.49E-03
100	1.149E-03	2.98E-03

Table 4.2. Flow rates for Geometry 1 under various zeta potential conditions with E = 100 V/cm.

Zeta	Q (mm^3/s)
$\zeta_{AC} = \zeta_B$	1.149E-03
$\zeta_{AC} = -\zeta_B$	9.189E-04
$\zeta_{AC}/\zeta_B = 0.5$	1.241E-03
$\zeta_B/\zeta_{AC} = 0.5$	1.636E-03

As can be seen from Table 4.1, the flow rates increase proportionally with an increase in electric field strength. Also, the converging-diverging section of the channel actually impedes the flow as the reference channel flow rates are approximately two to three times greater than Geometry 1.

Geometry 2

The velocity profiles of Geometry 2 (as well as Geometry 3) show the same trends as Geometry 1, that being that a balance of electrokinetic forces and pressure gradients will occur in the microchannel. When the zeta potentials are opposite one another, eddy's are generated in the microchannel that inhibits the flow greatly and in the case of Geometry 2, causes zero net flow.

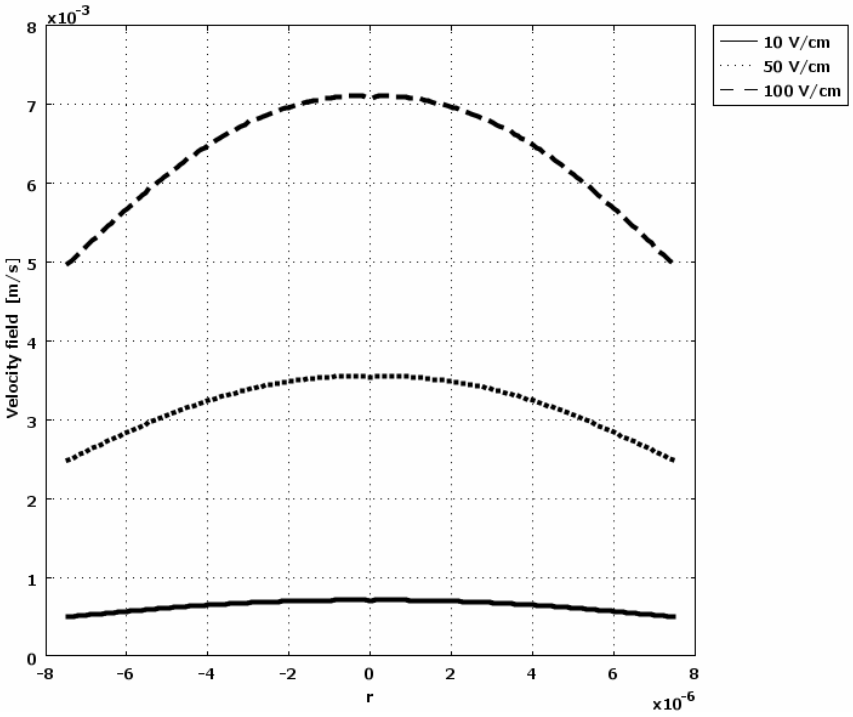

Figure 4.13. Velocity profile of Geometry 2 measured in section A for various electric field strengths with ζ = -100 mV.

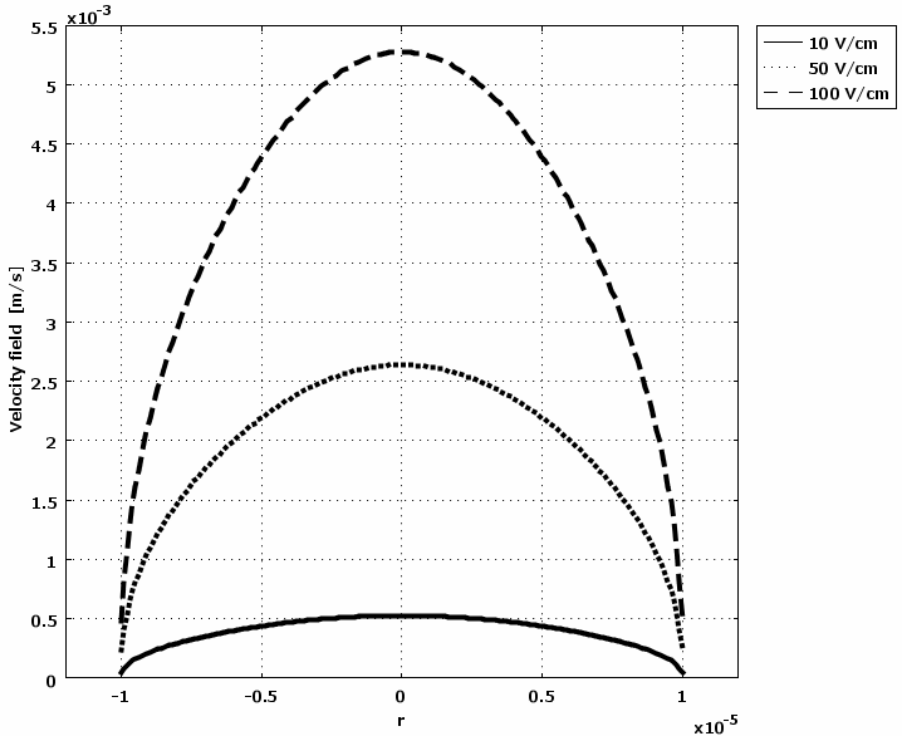

Figure 4.14. Velocity profile of Geometry 2 measured at the intersection of A and B for various electric field strengths with ζ = -100 mV.

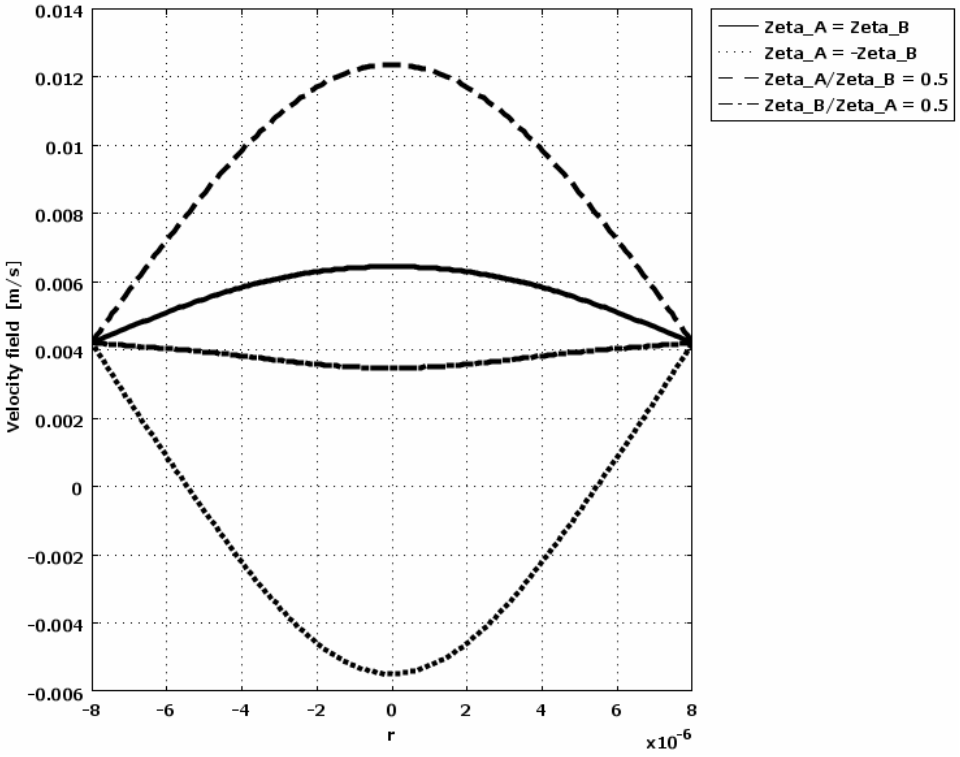

Figure 4.15. Velocity profile of Geometry 2 measured in section A for various zeta potentials with E = 100 V/cm.

Figure 4.15 shows a negative velocity magnitude due to backflow occurring in the microchannel when the zeta potentials in the respective areas are oppositve on another. The flow is positive near the channel wall, but actually becomes greatly negative in the middle of the channel as the flow has created an eddy and is moving in a circular pattern instead of flowing downstream.

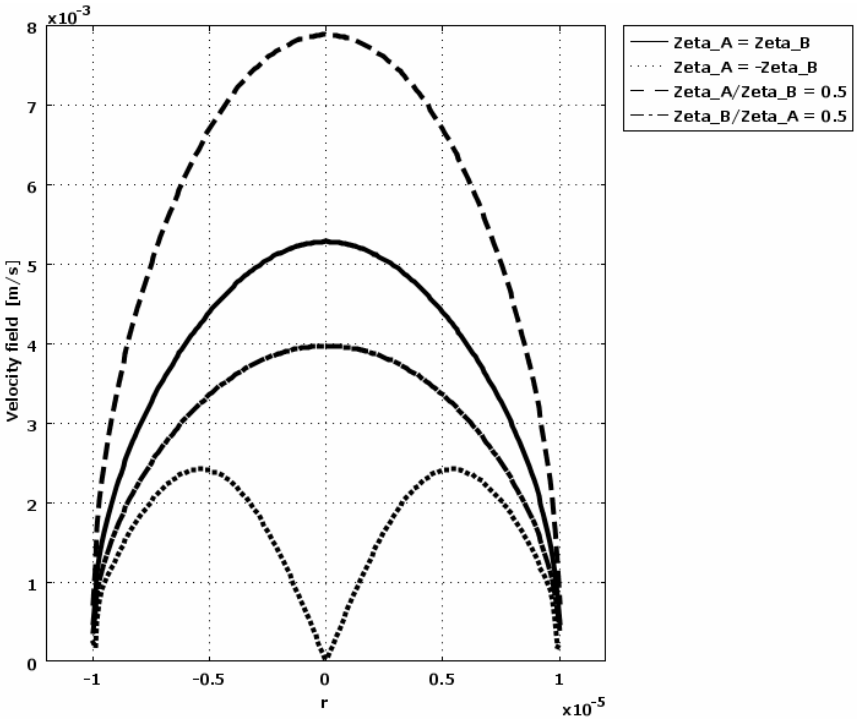

Figure 4.16. Velocity profile of Geometry 2 measured at the intersection of A and B for various zeta potentials with E = 100 V/cm.

In Figure 4.16, it can be seen that the velocity goes to zero in the middle of the channel when the zeta potentials are opposite one another. In fact, what has happened is eddy's are generated in the middle of the channel and at the interface between the two areas of opposite zeta charge, in the middle of the channel, there is no net flow moving in this section.

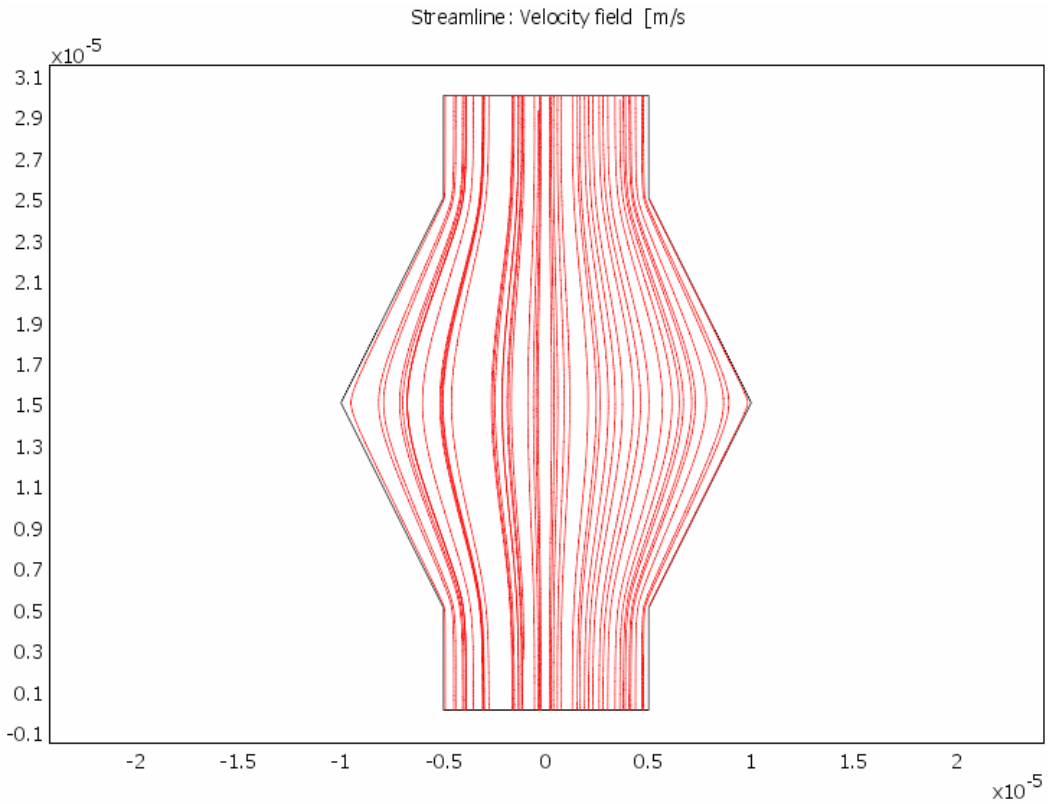

Figure 4.17. Streamlines of Geometry 2 in a homogeneous microchannel.

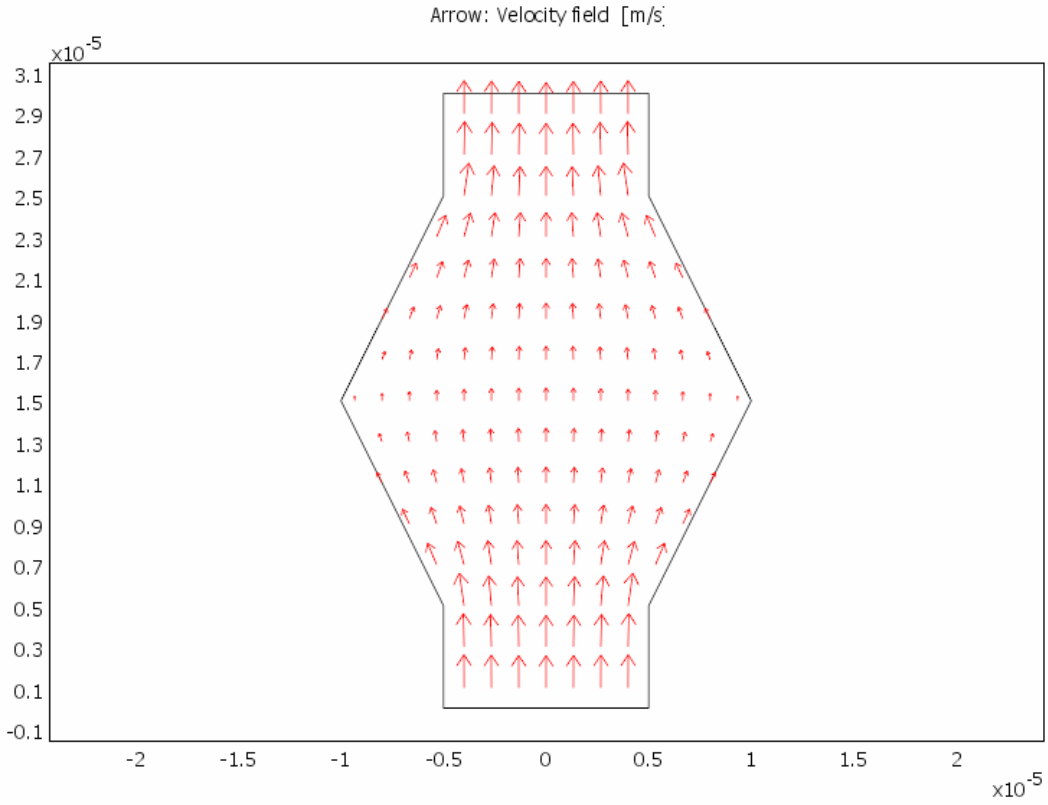

Figure 4.18. Arrow plot of Geometry 2 in a homogeneous microchannel.

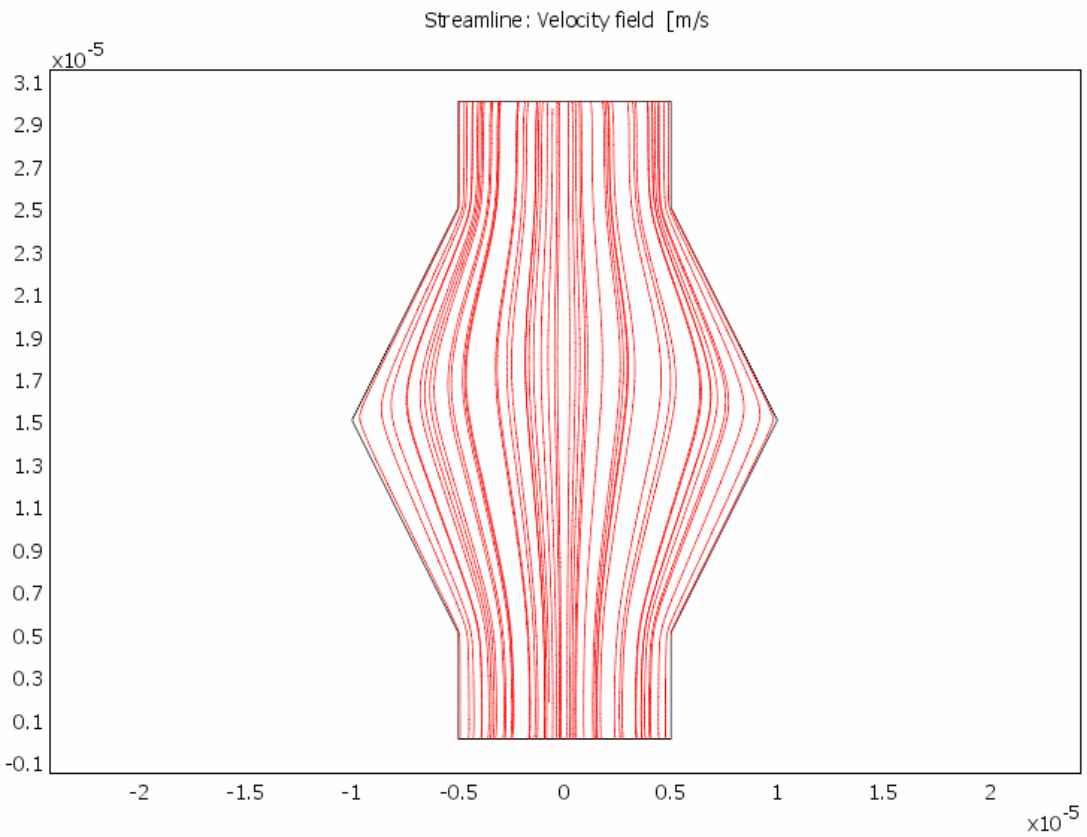

Figure 4.19. Streamlines of Geometry 2 with $\zeta_{AC}/\ \zeta_B = 2$.

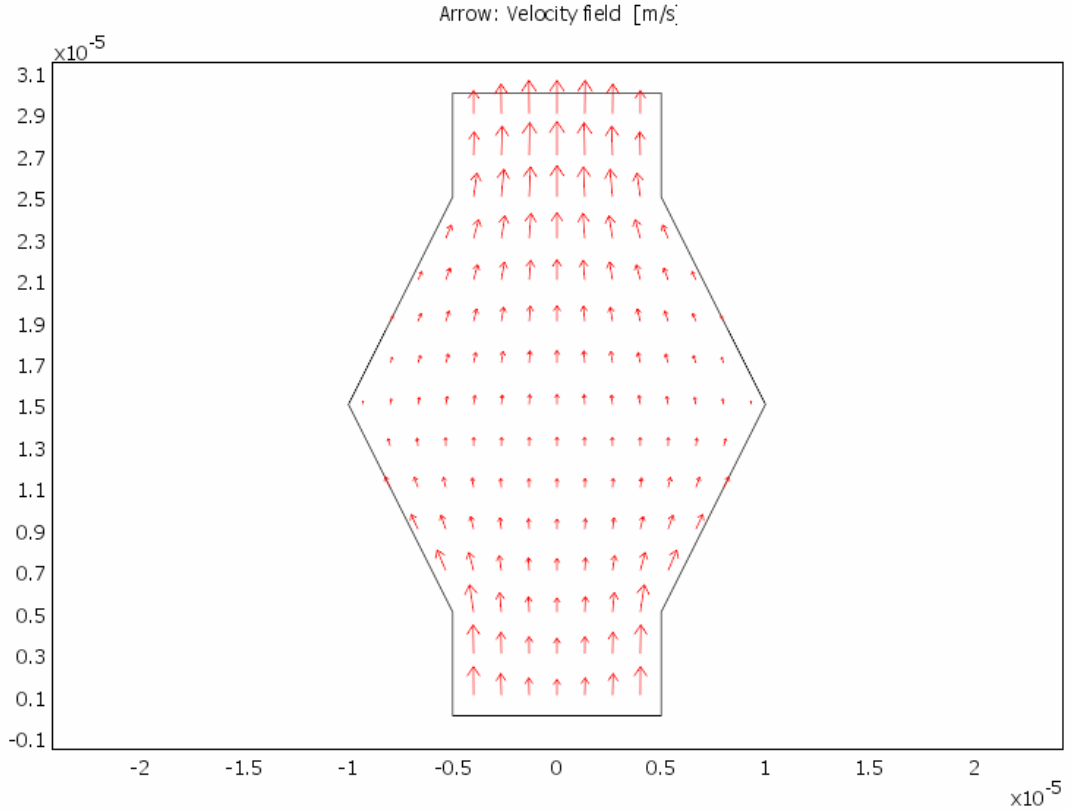

Figure 4.20. Arrow plot of Geometry 2 with $\zeta_{AC}/\ \zeta_B = 2$.

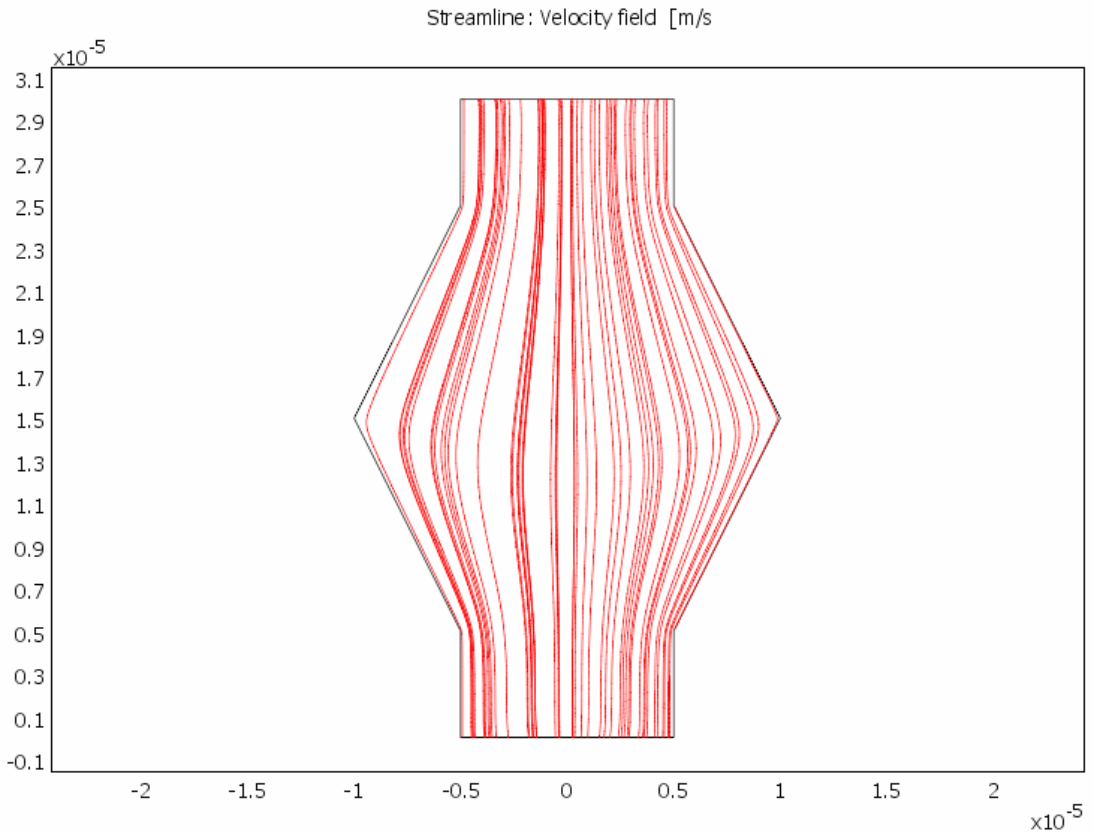

Figure 4.21. Streamlines of Geometry 2 with $\zeta_A/\ \zeta_B = 0.5$.

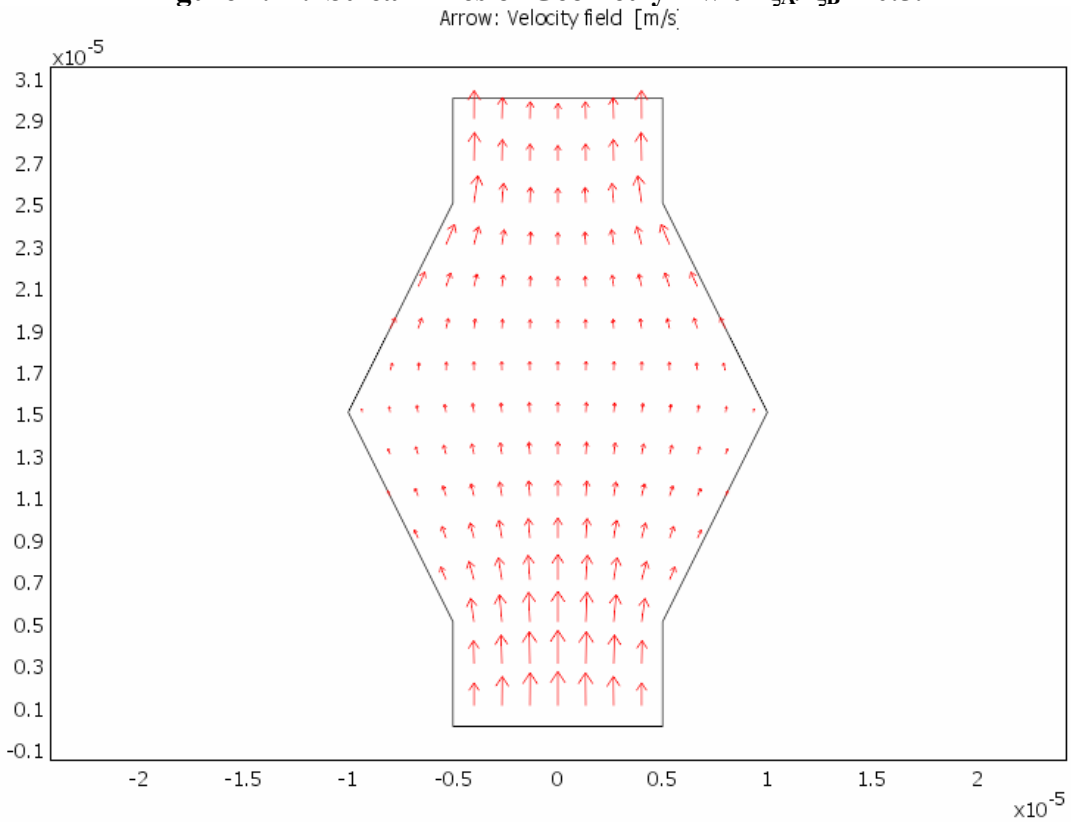

Figure 4.22. Arrow plot of Geometry 2 with $\zeta_A/\ \zeta_B = 0.5$.

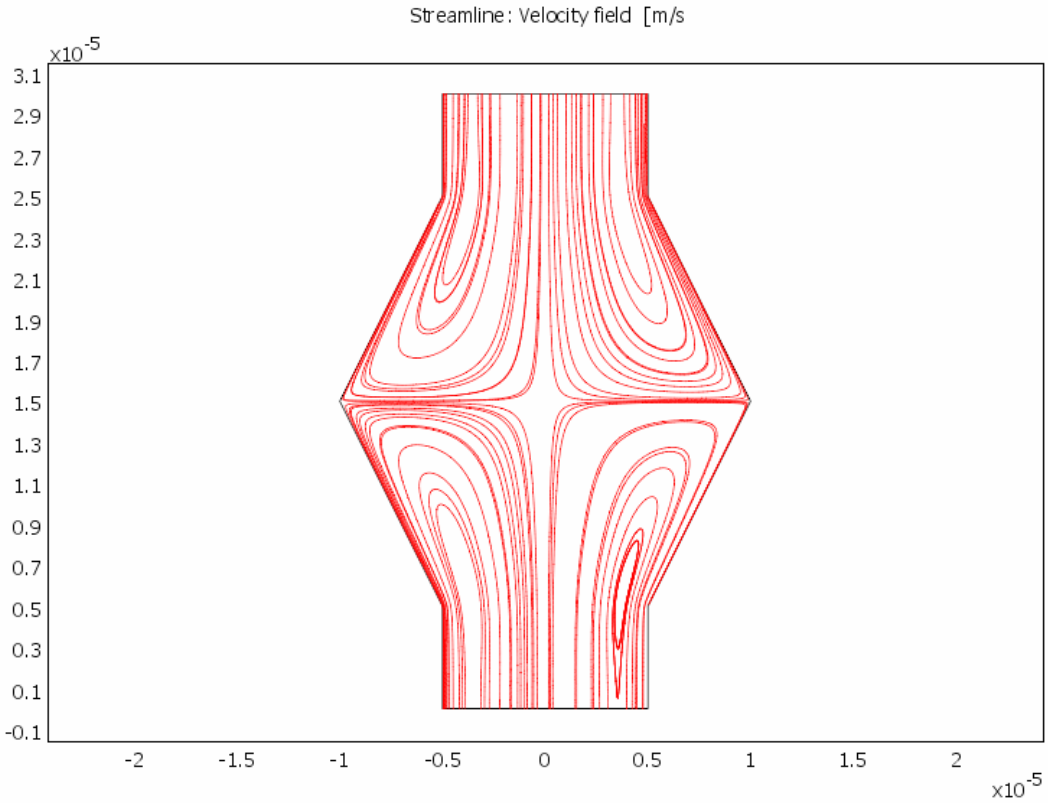

Figure 4.23. Streamlines of Geometry 2 with $\zeta_A = -\zeta_B$.

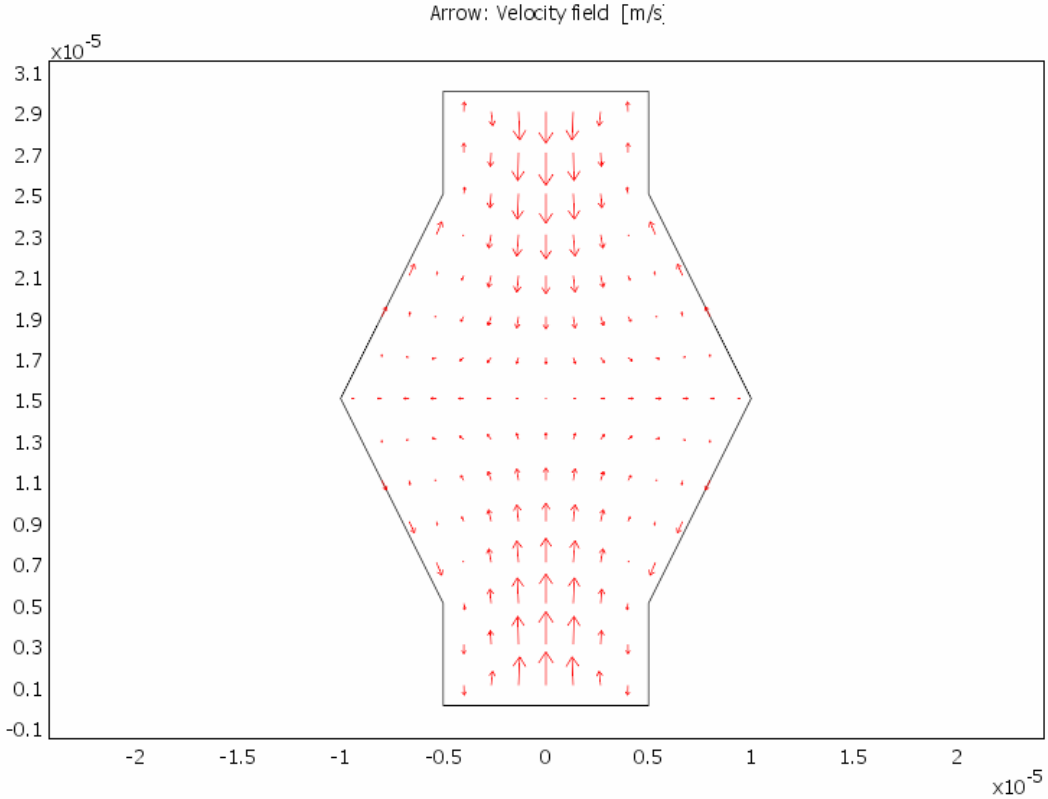

Figure 4.24. Arrow plot of Geometry 2 with $\zeta_A = -\zeta_B$.

Table 4.3. Flow rates for Geometry 2 under various applied electric field strengths with ζ = -100 mV, as well as reference geometry results.

E (V/cm)	G2 Q (mm^3/s)	Reference Q (mm^3/s)
10	1.060E-04	1.060E+05
50	5.301E-04	5.301E+05
100	1.060E-03	1.060E+06

Table 4.4. Flow rates for Geometry 2 under various zeta potential conditions with E = 100 V/cm.

Zeta	Q (mm^3/s)
$\zeta_{AC} = \zeta_B$	1.060E-03
$\zeta_{AC} = -\zeta_B$	0.000E+00
$\zeta_{AC}/\zeta_B = 0.5$	1.696E-03
$\zeta_B/\zeta_{AC} = 0.5$	8.482E-04

Geometry 3

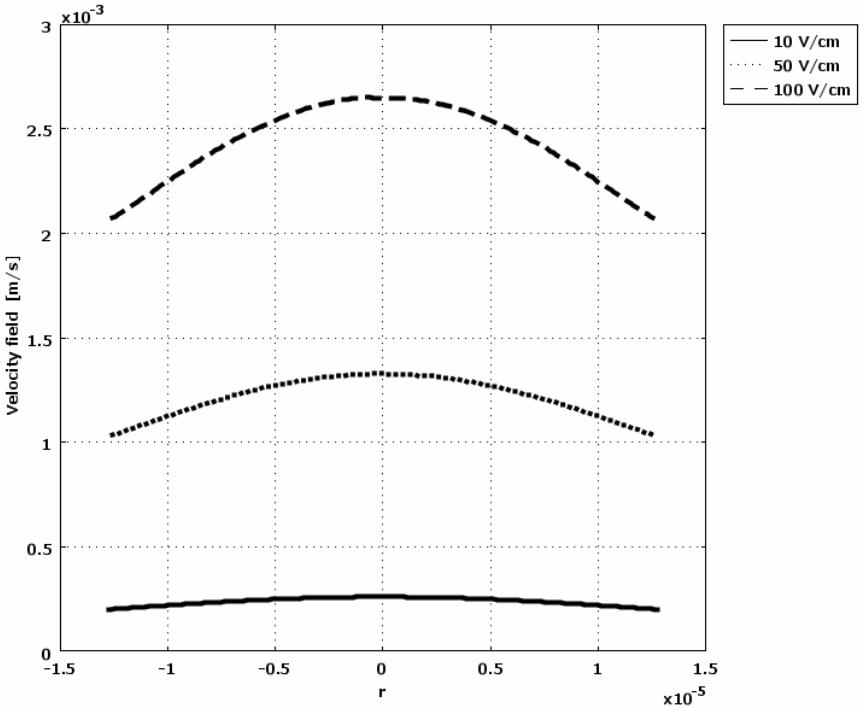

Figure 4.25. Velocity profile of Geometry 3 measured in section A for various electric field strengths with ζ = -100 mV.

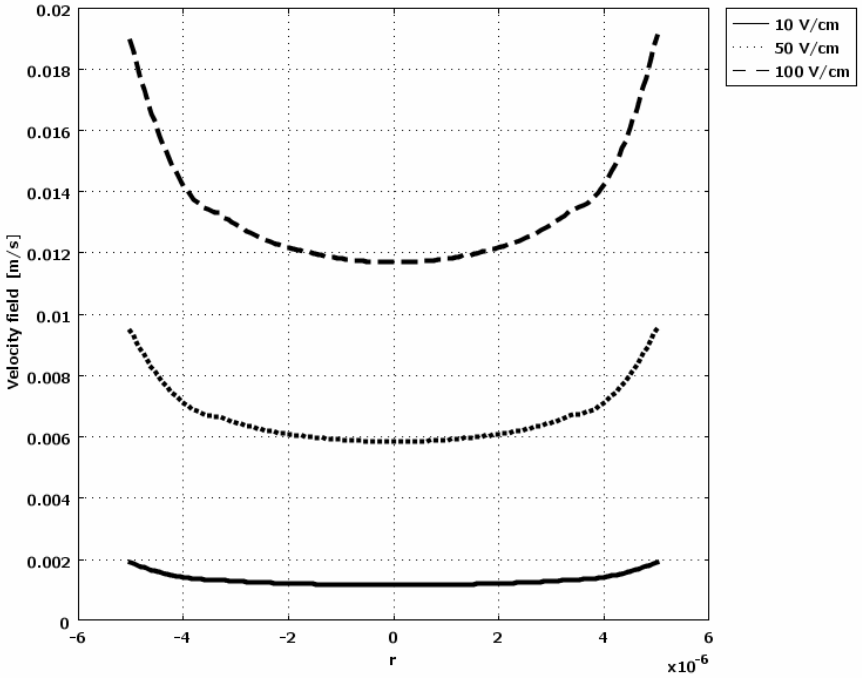

Figure 4.26. Velocity profile of Geometry 3 measured at the intersection of A and B for various electric field strengths with ζ = -100 mV.

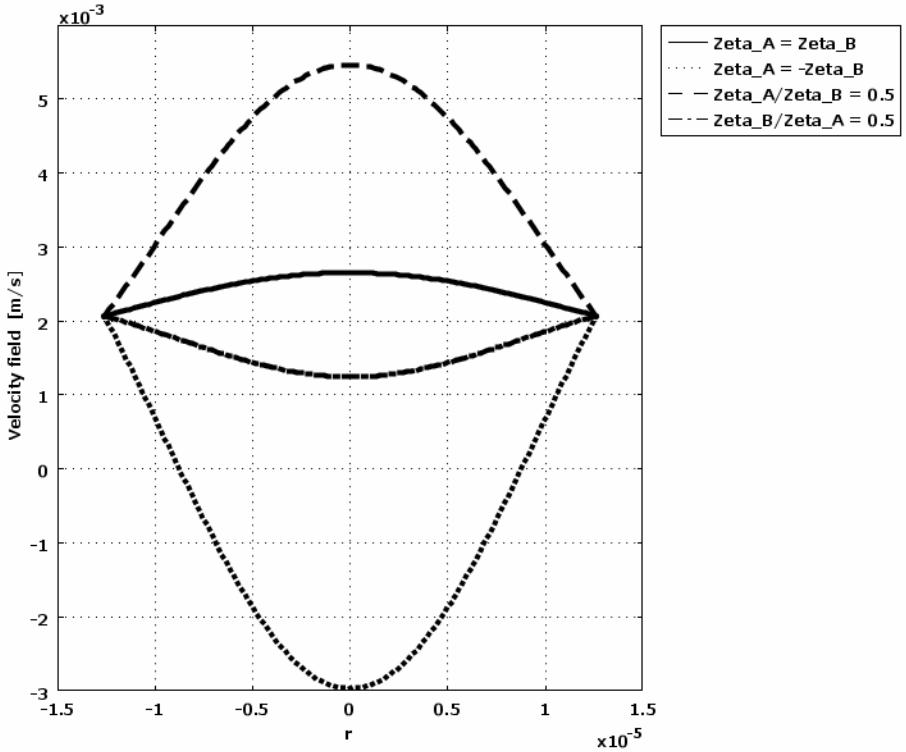

Figure 4.27. Velocity profile of Geometry 3 measured in section A for various zeta potentials with E = 100 V/cm.

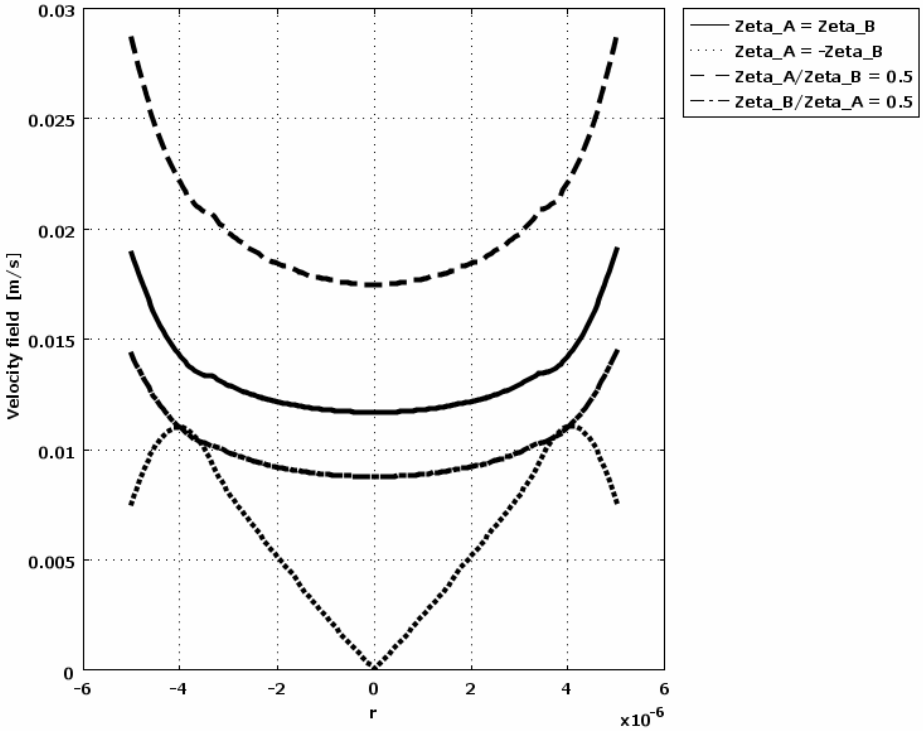

Figure 4.28. Velocity profile of Geometry 3 measured at the intersection of A and B for various zeta potentials with E = 100 V/cm.

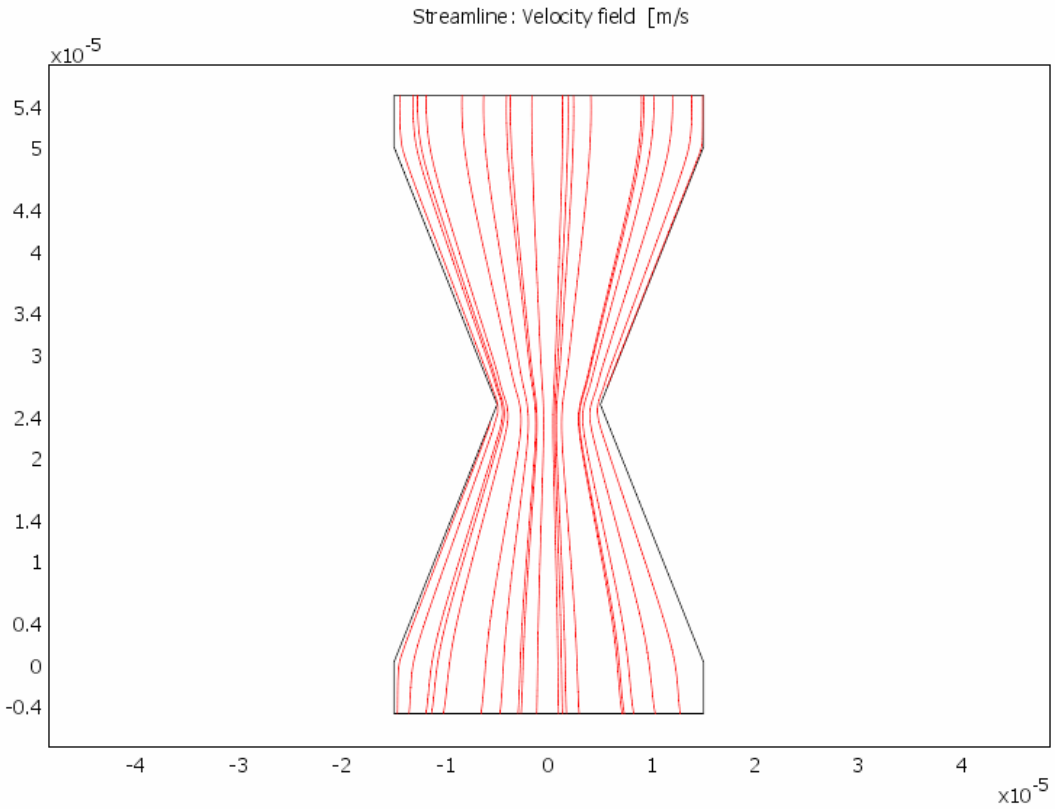

Figure 4.29. Streamlines of Geometry 3 in a homogeneous microchannel.

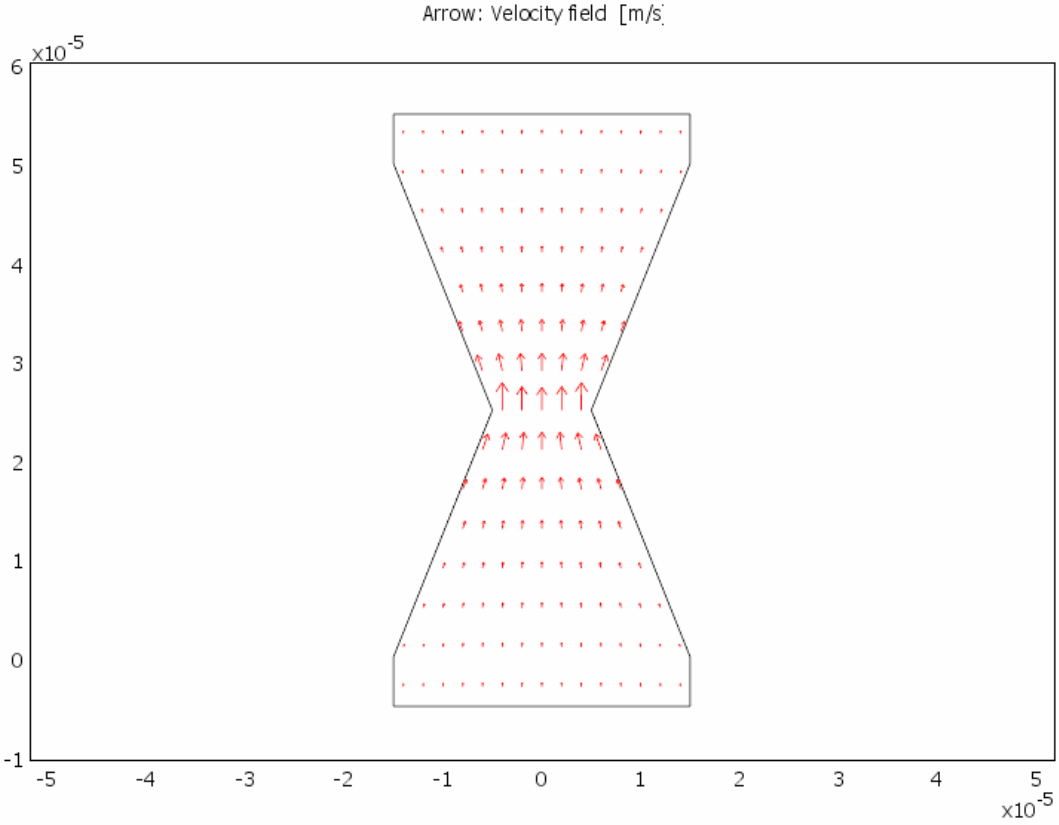

Figure 4.30. Arrow plot of Geometry 3 in a homogeneous microchannel.

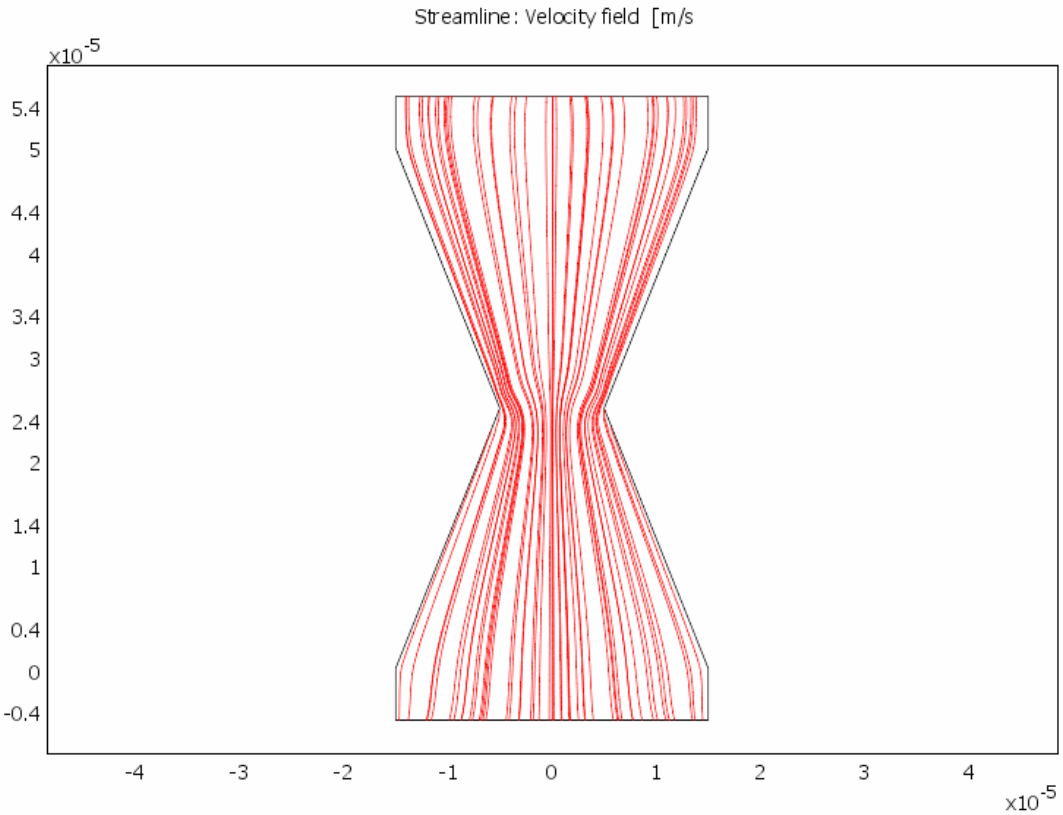

Figure 4.31. Streamlines of Geometry 3 with $\zeta_A/\zeta_B = 2$.

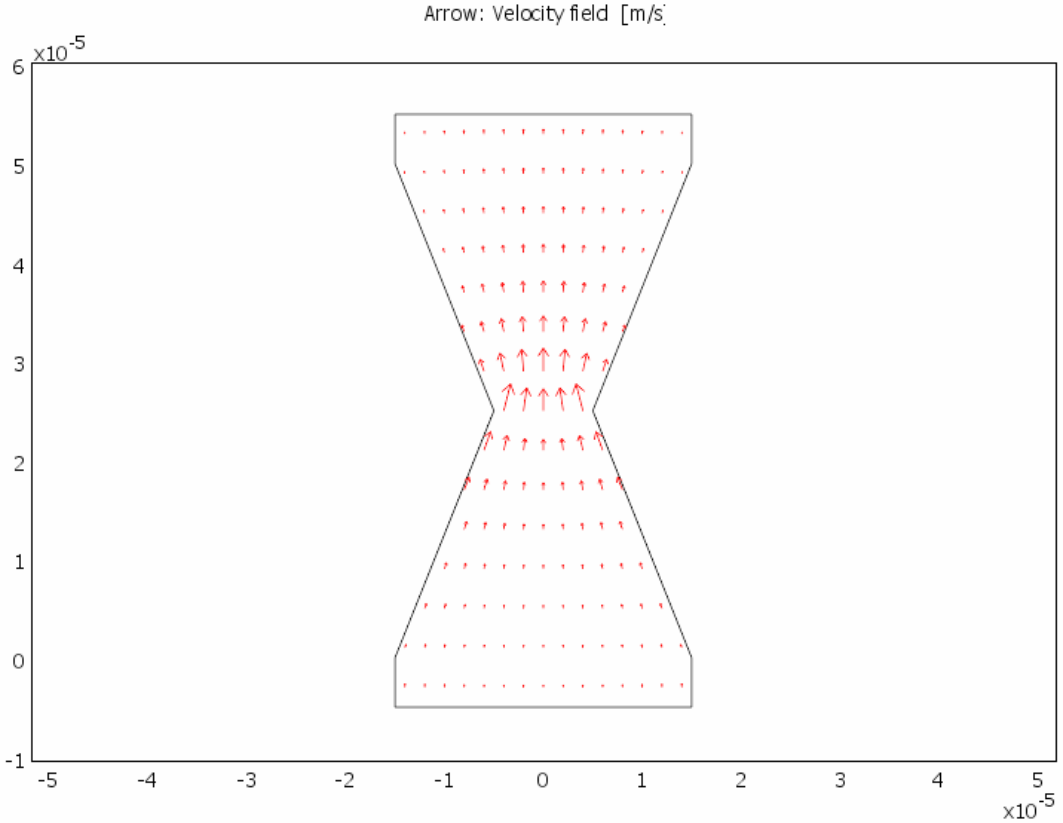

Figure 4.32. Arrow plot of Geometry 3 with $\zeta_A/\zeta_B = 2$.

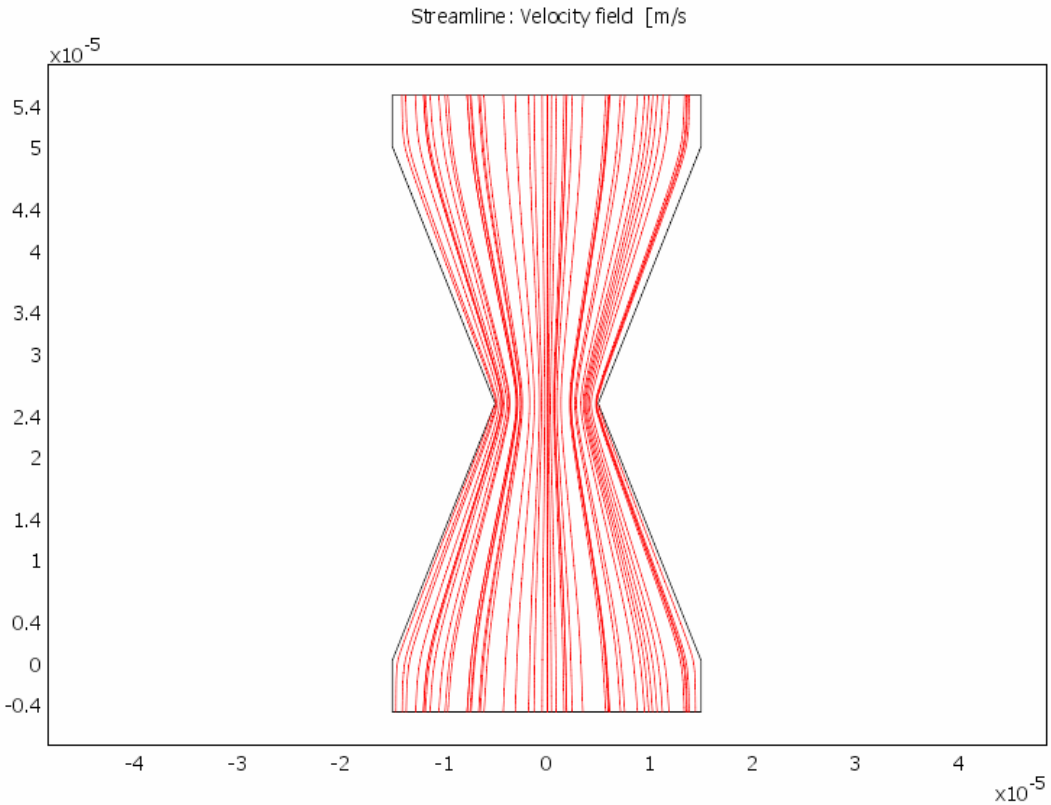

Figure 4.33. Streamlines of Geometry 3 with $\zeta_A/\ \zeta_B = 0.5$.

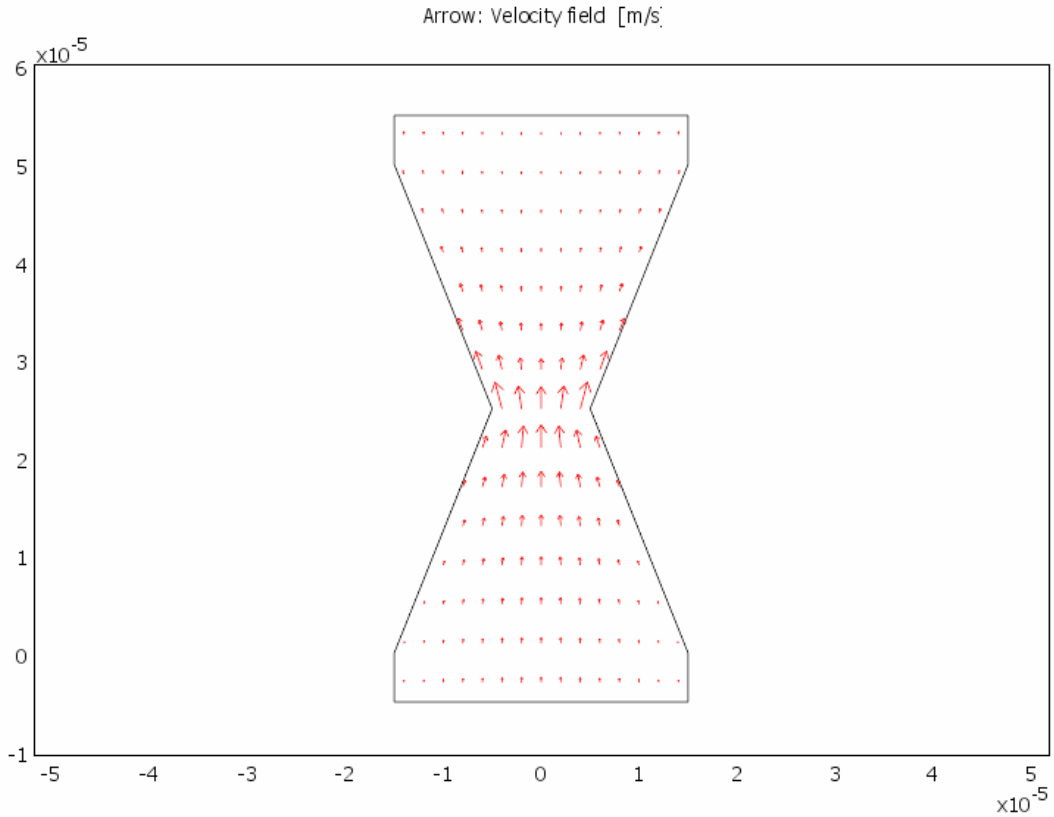

Figure 4.34. Arrow plot of Geometry 3 with $\zeta_A/\ \zeta_B = 0.5$.

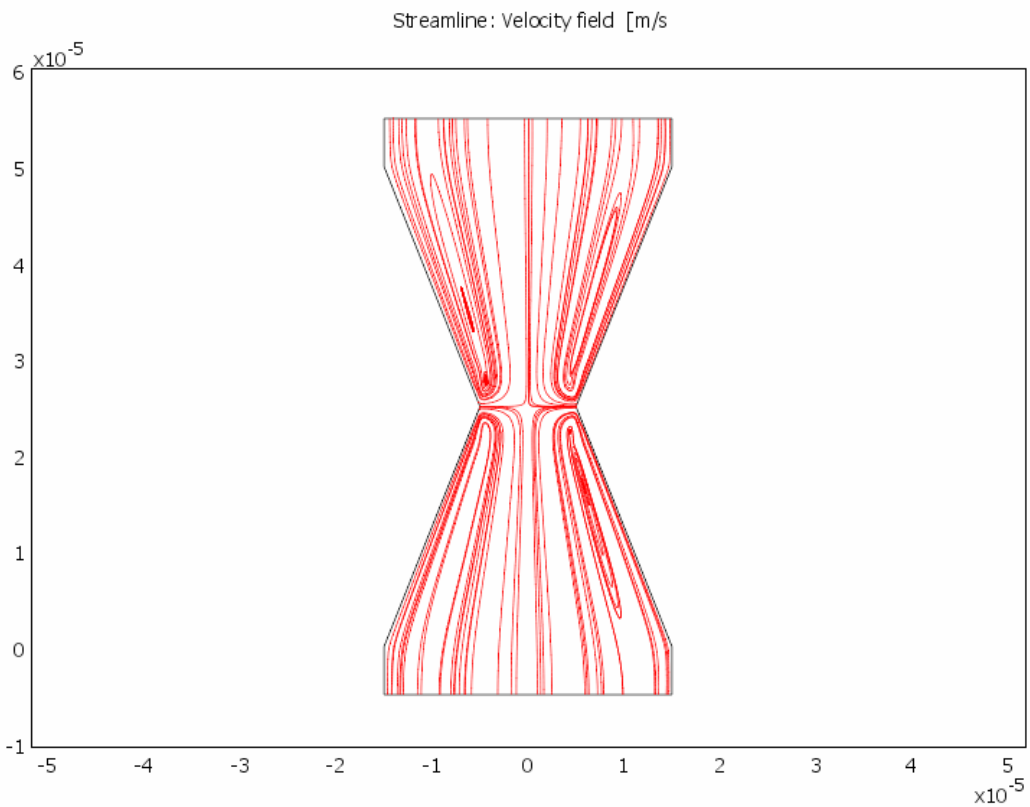

Figure 4.35. Streamlines of Geometry 3 with $\zeta_A = -\zeta_B$.

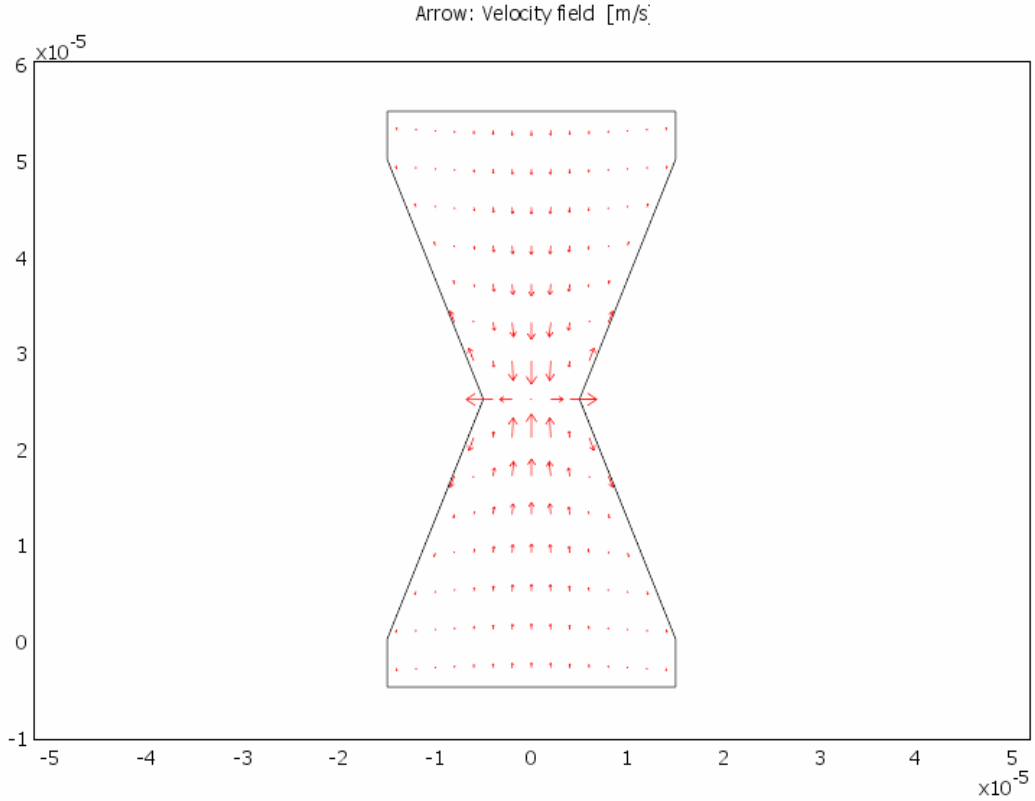

Figure 4.36. Arrow plot of Geometry 3 with $\zeta_A = -\zeta_B$.

Table 4.5. Flow rates for Geometry 3 under various applied electric field strengths with ζ = -100 mV, as well as reference geometry results.

E (V/cm)	G3 Q (mm^3/s)	Reference Q (mm^3/s)
10	9.425E-05	3.338E-04
50	3.770E-04	1.669E-03
100	7.069E-04	3.338E-03

Table 4.6. Flow rates for Geometry 3 under various zeta potential conditions with E = 100 V/cm.

Zeta	Q (mm^3/s)
$\zeta_{AC} = \zeta_B$	7.069E-04
$\zeta_{AC} = -\zeta_B$	5.655E-05
$\zeta_{AC}/\zeta_B = 0.5$	1.060E-03
$\zeta_B/\zeta_{AC} = 0.5$	4.807E-04

EDL Field

Apart from velocity profiles and streamlines, another area of concern is the EDL field. Previously, each geometry was modeled with the Helmholtz-Smoluchowski equation which allowed for simple results by neglecting the EDL field. Due to our specific cases (small EDL thickness, small change in radius direction), the EDL field in the geometries modeled would be the same as that of a circular capillary with constant-area. Thus, modeling the EDL field for all three geometries would produce the same results and be trivial. The only potential for differences however would be in the corners of the geometries where there is potential for overlap, such as the intersection of sections A and B for Geometry 2 and Geometry 3. However, this overlap effect could be considered negligible again due to the fact that the EDL is thin in comparison to the diameter of the microchannel. Thus, all EDL fields under these conditions would appear the same as that of Figure 4.37.

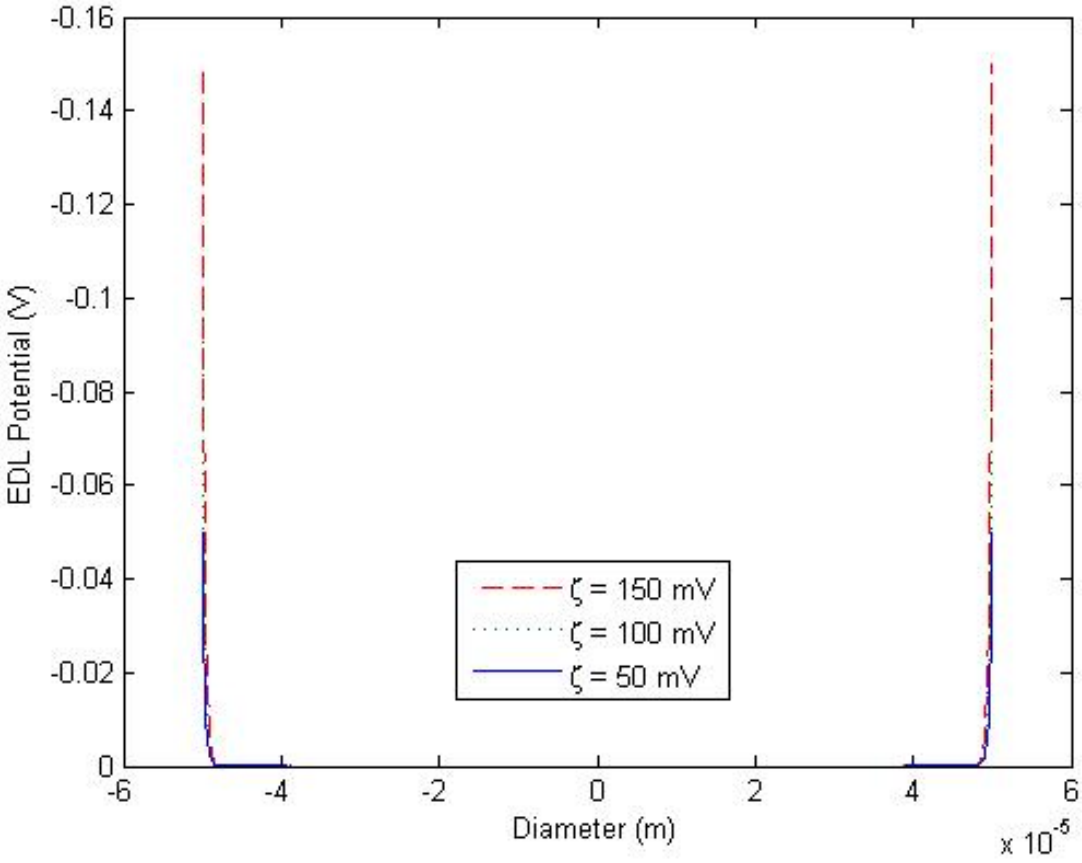

Figure 4.37. EDL field in a circular capillary microchannel.

CHAPTER V

CONCLUSIONS

Careful consideration of modeling electroosmotic flow in a heterogeneous converging-diverging microchannel show that three effects are taking place inside the microchannel that have significant consequences for the flow. The first effect is that applying an electric field along the length of the microchannel causes fluid to flow across a stationary charged surface. Increasing the applied electric field strength results in a proportional increase in velocity magnitude. The second effect is that the geometry of the microchannel affects the flow of an incompressible fluid due to the continuity equation, creating pressure gradients which can either increase or decrease the magnitude of the velocity. The geometries also play a considerable role in the shape of the velocity profile inside the microchannel. The third effect is that in a heterogeneous microchannel, pressure gradients generated at the interface of sections of different zeta potential can either advance or retard the flow. In heterogeneous cases where the zeta potentials are opposite, the flow is greatly retarded and in the case of Geometry 2, zero net flow occurs in the channel. Another effect of importance is that microchannels in which the downstream section of the channel had a greater zeta potential than the upstream section all produced the highest flow rates. Thus, the higher zeta potential attracts the fluid downstream faster and then moves it through its respective section faster than the opposite case, when the downstream section has a lower zeta potential.

In consideration of microchannel design, the designer must consider what the ultimate function of the microchannel is before considering these effects. If the microchannel is

designed to act as a mixer, then lower flow rates (giving more time for the two products to mix) would be more ideal, thus using a lower applied electric field strength and perhaps a lower zeta potential downstream. If the microchannel is to be used for cytometry purposes, then higher flow rates are probably more desirable and thus a higher applied electric field strength and higher zeta potentials downstream are more desirable. Ultimately, the designer must also consider how the use of different materials or fluids of varying pH may affect the flow inside the microchannel, as sections with opposite zeta potential have greatly retarded flow and in some cases, zero net flow. Thus, it is greatly desirable to avoid opposite zeta potential conditions when designing the channel.

REFERENCES

[1] Feynman, R.P., "There's Plenty of Room at the Bottom," *Journal of Microelectromechanical Systems,* Vol. 1, No. 1 (1992) 60-66.

[2] Moore, G., "VLSI, What Does the Future Hold," *Electron. Aust.,* Vol. 42, No. 14, (1980)

[3] Manz, A., Graber, N., and Widmer, H. M., "Miniaturized Total Chemical Analysis Systems: A Novel Concept for Chemical Sensing," *Sensors and Actuators B*, Vol. 1, (1990) 244-248.

[4] S.C. Jakeway, de Mello, A.J., Russell, and E.L., Fresenius, J., *Anal. Chem*., 366 (2000) 525-39.

[5] M.U. Kopp, de Mello, A.J., and Manz, A., *Science*, 280 (1998) 1046-8.

[6] Yang, J., Huang, Y., Wang, X.B., Becker, F.F., and Gascoyne, P.R., *Anal. Chem*., 71 (1999) 911-918.

[7] Oelschuk, R.D., Shultz-Lockyear, L.L., Ning, Y., and Harrison, D.J., *Anal. Chem.*, 72 (2000) 585-90.

[8] Erickson, D. and Li, D., *Langmuir*, 18 (2002) 1883-1892.

[9] Buchholz, B.A., et al., *Anal Chem.*, 73 (2001) 157-164.

[10] Glasgow, I.K., et al., *IEEE Transactions on Biomedical Engineering*, 48 (2001) 570-578.

[11] Folch, A., Jo, B.H., Hurtado, O., Beebe, D.J., and Toner, M., J. *Biomedical Materials Research*, 52 (2000) 346-353.

[12] Jacobson, S.C. and Ramsey, J.M., *Anal. Chem.*, 68 (1996) 720-3.

[13] Yang, T.L., Jung, S.Y., Mao, H.B., and Cremer, P.S., *Anal. Chem.*, 73 (2001) 165-169.

[14] Weigl, B.H., and Yager, P., *Science*, 283 (1999) 346-7.

[15] C.C. Wong, Development of a micro pump for microelectronic cooling, *Int. Mech. Eng. Congr. Expos.* (1996) 239-244.

[16] L.R. Arana, S.B. Schaevitz, A.J. Franz, M.A. Schmidt, K.F. Jensen, A micro fabricated suspended-tube chemical reactor for thermally efficient fuel processing, *J. MEMS* 12 (5) (2003) 600-612

[17] Reuss, F.F. *Memoires de la Societe Imperiale des Naturalistes de Moskou*, 2 (1809) 327

[18] S. Arulanandam and D. Li, *Colloids Surfaces A*, 161 (2000) 89

[19] J.P. Hsu, C.Y. Kao, S.J. Tseng and C.J. Chen, J. *Colloid Interface Science*, 248 (2002) 176.

[20] N.A. Patankar and H.H. Hu, *Anal. Chem.*, 70 (1998) 1870

[21] L. Hu, J. Harrison and J.H. Masliyah, J. *Colloid Interface Sci.*, 215 (1999) 300.

[22] F. Bianchi, R. Ferrigno and H.H. Girault, *Anal. Chem.*, 72 (2000) 1987.

[23] Xuan, X., Xu., B., and Li., D., *Anal. Chem.*, 77 (2005) 4323-4328

[24] Lee, J.S.H., Hu, Y., and Li, D., *Anal. Chim. Acta*, 543 (2005) 99-108

[25] Krishnamoorthy, S., Feng, J., Henry, A.C., Locascio, L.E., Hickman, J.J., Sundaram, S., *Microfluid Nanofluid*, 2 (2006) 345-355.

[26] Xuan, X., Raghibizadeh, S., Li, D., *Journal of Colloid and Interface Science* 296 (2006) 743-748.

[27] Herr, A.E., Molho, J.I., Santiago, J.G., Mungal, M.G., and Kenny, T.W., *Anal. Chem.*, 72 (2000) 1053-1057.

[28] Çetin, B. and Li, D., *Electrophoresis*, 29 (2008) 994-1005

[29] Li, D., *Electrokinetics in Microfluidics*, (2004) 103, Fig. 4.3.a.